

The Gaseous Environments of Quasars: Associate Absorption Lines with Density and Distance Constraints

Chen Chen,^{1,2★} Fred Hamann,² Leah Simon^{3,1} and Thomas Barlow⁴

¹*Department of Astronomy, University of Florida, 211 Bryant Space Science Center, FL 32611, USA*

²*Department of Physics & Astronomy, University of California, Riverside, CA 92521, USA*

³*Hands On Labs, 750 W. Hampden Ave., Suite 100, Englewood, CO 80110*

⁴*Caltech Optical Observatories, 1200 E California Blvd, Pasadena, CA 91125, USA*

ABSTRACT

Associated absorption lines (AALs) in quasar spectra are valuable probes of the gas kinematics and physical conditions in quasar environments. The host galaxies are by definition in an active evolution stage that might involve large-scale blowouts and/or cold-mode accretion (infall) from the intergalactic medium (IGM). We discuss rest-frame UV spectra of four redshift 2–3 quasars selected to have low-ionisation AALs of Si II or C II that place unique density and distance constraints on the absorbers. Our analysis of the AALs yields the following results. One of the quasars, Q0119–046, has a rich complex of 11 AAL systems that appear to be infalling at measured speeds from ~ 0 to ~ 1150 km s⁻¹ at distance ~ 5.7 kpc from the quasar. The range of ions detected, up to Ne VIII, indicates a wide range of densities from ~ 4 to ~ 2500 cm⁻³. Partial covering the quasar emission source requires cloud sizes < 1 pc and possibly < 0.01 pc. The short dissipation times of these small clouds suggests that they are created in situ at their observed location, perhaps as dense condensations in cold-mode accreting gas from IGM. The AALs in the other three quasars have outflow speeds from ~ 1900 to ~ 3000 km s⁻¹. Some of them also appear to have a range of densities based on the range of ions detected, including Mg I $\lambda 2853$ in Q0105+061. However, the absence of excited-state AALs yields only upper limits on their gas densities ($\lesssim 150$ cm⁻³) and large minimum distances ($\gtrsim 40$ kpc) from the quasars. These AALs might represent highly extended quasar-driven outflows, although their actual physical relationships to the quasars cannot be established.

Key words: galaxies: evolution – quasars: absorption lines – quasars: general

1 INTRODUCTION

High-redshift quasars in the centers of massive galaxies signal an active early stage of massive galaxy evolution. Popular evolution models suggest that the black hole accretion that defines quasar activity is accompanied by a rapid burst of star formation in the host galaxies, triggered perhaps by a galaxy merger or interaction (Sanders et al. 1988; Elvis 2006; Hopkins et al. 2008; Veilleux et al. 2009; Hopkins et al. 2016). This activity is expected to continue until powerful outflows (feedback) driven by the central quasar and/or star formation lead to a blowout of gas and dust that quenches the starburst and cuts off the fuel supply for black hole accretion (Silk & Rees 1998; Kauffmann & Haehnelt 2000; King 2003; Scannapieco & Oh 2004; Di Matteo, Springel & Hernquist 2005; Ostriker et al. 2010; Debuhr, Quataert & Ma

2012; Rupke & Veilleux 2013; Rupke, Gültekin & Veilleux 2017; Cicone et al. 2014).

Infalling gas from the intergalactic medium (IGM, e.g., cold mode accretion) is also expected to be important during the early evolution stages to build galaxy mass, trigger star formation, and fuel the central black holes (Katz et al. 2003; Kereš et al. 2009, 2012). Recent observations show that massive gas reservoirs are indeed present around high-redshift quasars, and that they are more extended and more massive around quasar hosts than similar inactive (non-quasar) galaxies (e.g., Prochaska, Lau & Hennawi 2014; Johnson, Chen & Mulchaey 2015; Martin et al. 2015, 2016; Borisova et al. 2016; Bouché et al. 2016; Ho et al. 2017). These gas reservoirs are consistent with enhanced infall/cold-mode accretion from the IGM during the early/active quasars stages of massive galaxy evolution. It is likely that infall and outflow occur together if cold-mode accretion is involved in triggering the starbursts and quasars that also drive feedback

★ E-mail: chenomvmjs@ufl.edu

(Costa, Sijacki & Haehnelt 2014; Nelson et al. 2015; Suresh et al. 2015).

Associated absorption lines (AALs) in quasar spectra are unique tools to study the gaseous environments of quasars and test models of massive galaxy evolution. AALs have narrow velocity widths (less than a few hundred km s^{-1}) much different from broad absorption lines (BALs), whose velocity widths $\gtrsim 2000 \text{ km s}^{-1}$ clearly identify high-speed quasar-driven outflows (Anderson et al. 1987; Weymann et al. 1991; Hamann & Sabra 2004; Simon & Hamann 2010; Muzahid et al. 2013). The term "associated" means they have absorption redshifts within several thousand km s^{-1} of the quasar emission-line redshift (i.e., $z_{abs} \approx z_{em}$, Weymann et al. 1979; Foltz et al. 1986; Hamann 1997). It is known from statistical studies of large quasar samples that most AALs are intrinsic to the quasars, i.e., they form broadly within the environment of the quasar or its host galaxy (Nestor, Hamann & Rodriguez Hidalgo 2008; Wild et al. 2008; Perrotta et al. 2016). However, AALs can have a wide range of physical origins, from outflows near the quasars, to extended halos in the host galaxies, to cosmologically intervening gas or galaxies unrelated to the quasars (Sargent, Boksenberg & Young 1982; Tripp, Lu & Savage 1996; Hamann et al. 2001; D'Odorico et al. 2004; Hamann et al. 2011).

Several observational tests have been proposed to determine if individual AAL systems are likely intrinsic (Barlow, Hamann & Sargent 1997; Hamann, Barlow & Junkkarinen 1997; Hamann & Ferland 1999; Ganguly et al. 1999; Wise et al. 2004; Narayanan et al. 2004; Misawa et al. 2007b). They include 1) high gas densities inferred from excited-state absorption lines (that require a close proximity to the quasars based on photoionisation constraints), 2) absorption line variability, 3) partial covering of the background light source that, for quasars, requires very small absorbing clouds, and 4) line profiles indicative of gas flows because they are too broad and smooth compared to thermal velocities (see also Hamann & Ferland 1999; Srianand & Petitjean 2000; Schaye, Carswell & Kim 2007; Ganguly et al. 1999; Arav et al. 2008). These properties tend to go together. They are indicative of an intrinsic origin because they are more readily understood in terms of the dense dynamic of quasars compared to the larger, more quiescent, and lower density clouds expected for intervening absorption (Rauch 1998).

In this paper, we describe a study to understand the nature and origins of low-density associated absorbers that might reside in the extended host galaxies of quasars. This is an interesting subset of AALs because the extended galactic environments are where we might find evidence for cold mode accretion or quasar-driven winds directly interacting with the galactic interstellar medium. We describe the quasar sample and the data used in Section 2. We fit the AALs to measure the kinematics, column densities, and covering fractions in Section 3. We analyze the physical properties including ionisation, electron density, metallicity and radial distance in Section 4, and in Section 5 we discuss the origins and dynamics of absorption-line clouds. We conclude with a summary in Section 6. Throughout this paper, we adopt a cosmology with $H_0 = 71 \text{ km s}^{-1} \text{ Mpc}^{-1}$, $\Omega_M = 0.27$ and $\Omega_\Lambda = 0.73$.

2 DATA OVERVIEW

2.1 Quasar Sample

We select four AAL quasars for our study from samples observed previously by our team using the High Resolution Echelle Spectrometer (HIRES) at the W. M. Keck Observatory (Keck) or the Ultraviolet and Visual Echelle Spectrometer (UVES) at the ESO Very Large Telescope (VLT). We require that the quasars have low-ionisation AALs of C II or Si II detected in these existing high-resolution spectra. This sample is not intended to be representative of all quasar AALs. In particular, the low-ionization C II and Si II lines are rare in AAL systems. However, these lines place unique constraints on the absorber densities and locations. They can, therefore, provide unique insights in the nature of the gas flows around quasars and their extended host galaxies.

The quasars, their redshifts, and some basic information about the data are listed in Table 1. Q0105+061, Q0334–204, and Q2044–168 are the only quasars with detected C II or Si II AALs in the larger sample of 24 AAL quasars described by Simon, Hamann & Pettini (2012). The 24 AAL quasars were selected from the Sloan Digital Sky Survey (SDSS) to be bright (apparent Magnitude $\lesssim 19$) with C IV AALs at redshifts $\gtrsim 2$. Q0119–046 is selected from unpublished high-resolution spectra obtained with both Keck and the Hubble Space Telescope (HST). Q0119–046 and Q2044–168 are radio-loud (Murphy et al. 2010; Chhetri et al. 2013), while Q0105+061 and Q0334–204 are radio-quiet (Sramek & Weedman 1980; Robson et al. 1985). The AALs in Q0119–046 were studied previously by Sargent, Boksenberg & Young (1982). Here we present data with higher spectral resolution and higher signal-to-noise ratios, with wider wavelength coverage in the HST data that reveals additional absorption lines including Ne VIII $\lambda 770$, 780, O VI $\lambda 1032$, 1038, and the Lyman lines to yield important new results on the nature of its AAL absorbers.

Accurate systemic redshifts are important to judge infall versus outflow for the AALs and estimate the outflow kinetic energies. Redshifts derived from UV broad emission lines are known to be uncertain because the lines can be shifted in the quasar frame, with different lines shifted by different amounts. High-ionisation lines like C IV $\lambda 1548, 1551$ are typically blueshifted by several hundred km s^{-1} compared to narrow forbidden lines such as [O III] $\lambda 5007$, which is generally regarded to be the best UV/optical indicator of quasar systemic redshifts (Gaskell 1982; Shen et al. 2007; Wang et al. 2011). Low-ionisation permitted lines such as Mg II $\lambda 2800$ can also be good redshift indicators because their shifts relative to [O III] are typically $\sim 100 \text{ km s}^{-1}$ (Richards et al. 2002). We search the literature to find the best available redshift for each quasar based on the lines measured and the data quality. The results are listed in Table 1. Below are some specific notes.

Q0105+061: Ulrich (1989) performed Gaussian fit (two-component fits for double lines) to measure the emission lines C IV, C III] $\lambda 1909$, and Si IV+O IV] $\lambda 1398$ in the spectrum with resolution 7 \AA . The redshifts are 1.955, 1.953, 1.965, respectively, from the measurements of the three emission lines. We adopt $z_{em} = 1.960 \pm 0.005$ ($\pm 507 \text{ km s}^{-1}$) by weighting their individual line measurements based on the emission line widths.

Q0119–046: Steidel & Sargent (1991) measured Mg II to

Table 1. Quasar data including the name, emission-line redshift, telescope-instrument used for observations, observation date (dd/mm/year), rest wavelength ranges, and spectral resolution $R = \lambda/\Delta\lambda$.

Quasar	z_{em}	Instrument	Obs. Date	λ_{rest} (Å)	R
Q0105+061	1.960 ^a	VLT-UVES	09/22/2003	1184-1604 2044-3352	80000 110000
Q0119-046	1.9635 ^b	Keck-HIRES	03/12/1996	1147-1989	45000
		HST-FOS	09/24/1996	750-1106	1300
Q0334-204	3.132 ^c	VLT-UVES	09/23/2003	848-1077 1152-1654	80000 110000
Q2044-168	1.939 ^d	VLT-UVES	09/22/2003	1193-1606 2059-3376	80000 110000

^a Ulrich (1989)

^b Steidel & Sargent (1991)

^c Tytler & Fan (1992)

^d Tytler et al. (2004)

determine the emission-line redshift $z_{em} = 1.9635$ by calculating the flux-weighted mean wavelength of the line above 85% of its peak height. Given the spectral resolution and noise in the data, they estimated that the errors on their line positions are typically ~ 50 – 100 km s⁻¹. We adopt the value 1.9635 ± 0.0020 (± 202 km s⁻¹), with a generous uncertainty to include the measurement uncertainty and the typical offset, ~ 100 km s⁻¹, of Mg II relative to [O III] emission lines (Richards et al. 2002; Shen et al. 2007).

Q0334-204: Tytler & Fan (1992) presented a new maximum-likelihood method, which gave more accurate results than previous studies, to measure emission lines of Ly α λ 1216, Si IV+O IV], C IV, and C III]. They obtained a value of 3.1322 ± 0.0013 (± 94 km s⁻¹). We directly use this redshift.

Q2044-168: Tytler et al. (2004) measured the emission-line redshifts using lines Ly α , N V λ 1240, Si IV+O IV], C IV, C III] with a typical error of 5 Å for the peak wavelengths, and the redshifts determined by these lines are 1.939, 1.939, 1.936, 1.939, 1.938, respectively. We adopt the value of 1.939 ± 0.001 (± 102 km s⁻¹) by weighting their individual line measurements.

2.2 Observations and Data Reduction

Basic information about the observations is listed in Table 1. Spectra of Q0119-046 were observed with High Resolution Echelle Spectrometer (HIRES) on Keck and Faint Object Spectrograph (FOS) on the HST. The other three quasars were observed with UV-Visual Echelle Spectrograph (UVES) on the VLT. All of the spectra cover important absorption lines from at least Ly α λ 1216 to C IV λ 1548, 1551 in the quasar rest frame. The HST-FOS spectrum of Q0119-046 provides additional UV coverage below the Lyman limit. The wavelength scales throughout this paper are vacuum heliocentric. We used standard techniques to reduce the Keck-HIRES and VLT-UVES spectra. In particular, for the Keck-HIRES spectra, we used a software package MA-

KEE (as described in Barlow & Sargent 1997; Hamann et al. 1997b) for initial data reduction and spectral extraction. These procedures are described in detail in Hamann et al. (2001). The VLT-UVES data reduction procedures are described in Simon (2011).

We use the IRAF¹ software package for additional data processing. In particular, we normalize the reduced Keck and VLT spectra to unity by fitting a pseudo-continuum to each quasar spectrum, including the emission lines. For regions with few absorption lines, we apply a polynomial fit locally around the absorption lines we will measure for our study. For the regions where the continuum is affected by significant absorption, e.g., in the Ly α forest, we visually inspect the spectra to find small segments of continuum not affected by absorption or obvious noise spikes. We then interpolate between these segments, fitting the entire region with a low order polynomial.

2.2.1 HST-FOS Spectrum of Q0119-046

For Q0119-046 only, we include the UV spectrum obtained with HST-FOS shown in Figure 1. We retrieved this spectrum already reduced and calibrated from the Mikulski Archive for Space Telescopes (MAST). We attempted to test the wavelength calibrations using the Galactic absorption lines of Mg II λ 2796, 2804 and Fe II λ 2587, 2600 (Schneider et al. 1993). However, these lines are contaminated in the Ly α forest and not useful. Instead, we compare the Ly α AALs measured in the Keck spectrum (labeled as 2 and 7 in Figure 3) to the corresponding Ly β , Ly γ and Ly δ AALs in the HST spectrum (labeled as 2* and 7* in Figure 3). Our fits to these lines (described below) show no significant differences in the centroid redshifts and, therefore, we do not apply any corrections to the HST spectrum wavelengths.

The HST spectrum has a much lower resolution than the Keck spectrum, but it covers shorter wavelengths with a variety of important AALs, including Ne VIII λ 770, 780, O VI λ 1032, 1038, and the Lyman lines, plus strong Lyman limit absorption at the same redshift. Figure 1 shows our estimates of the continuum on either side of the Lyman edge (912 Å). These continuum estimates are simple power laws of the form $F_\lambda \propto \lambda^\alpha$, with a Gaussian profile added at ~ 1034 Å in the quasar frame to account for the broad O VI λ 1032, 1038 emission line. The AALs and numerous unrelated Ly α forest lines make it difficult to locate the true continuum. We constrain our fits to using the median flux in narrow wavelength windows that appear relatively free of absorption lines. At wavelengths > 912 Å, the continuum slope near the Lyman edge is not well constrained due to absorption-line blending. We therefore consider three different continua (shown by the colored curves in Figure 1) that are upper and lower limits and a best-guess middle case based on visual inspection.

¹ Image Reduction and Analysis Facility (IRAF) is maintained and distributed by the National Optical Astronomy Observatories.

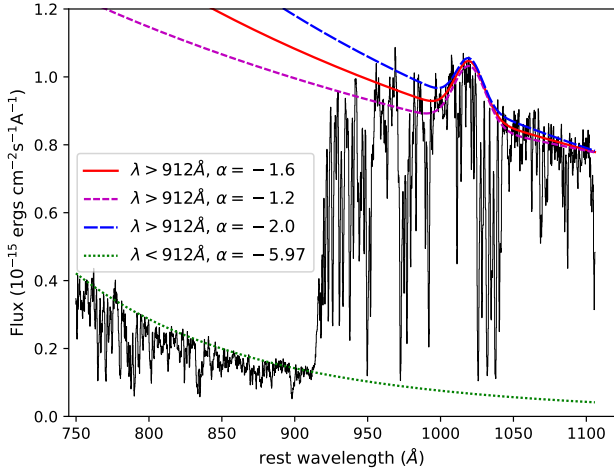


Figure 1. HST spectrum of Q0119–046. The dotted green line shows the fit of the continuum at $\lambda < 912 \text{ \AA}$, and the solid red line shows the best estimation of the continuum at $\lambda > 912 \text{ \AA}$, including O VI emission line. The dashed blue and mauve lines show upper and lower limits at $\lambda > 912 \text{ \AA}$, respectively.

3 ABSORPTION FEATURES

3.1 Line Identifications

Figures 2 to 6 show the AAL profiles for all four quasars on a velocity scale relative to the emission-line redshifts. All of the quasars have multiple or complex/blended AAL systems. We identify individual AAL systems starting with the C IV $\lambda 1548, 1551$ and Si IV $\lambda 1394, 1403$ doublets because these lines are not contaminated in Ly α forest and they tend to be strong and well-measured at wavelengths with high signal-to-noise ratios in our spectra. If these lines are broad or blended with neighboring features, we use weaker lines such as C II $\lambda 1335$ and Si II $\lambda 1260, 1304, \text{ and } 1527$, if available, to identify individual components and measure redshifts for the system. We then search other lines at these same redshifts. For Q0119–046, the search for additional lines includes the HST-FOS spectrum down to $\sim 750 \text{ \AA}$ in the quasar rest frame. The lines identified in each quasar are listed in Tables 2 to 6 below. We now describe the line measurements and the contents of these data tables.

3.2 Line Profile Fits

We fit each AAL with a Gaussian optical depth profile given by,

$$\tau_v = \tau_0 e^{-v^2/b^2}, \quad (1)$$

where τ_v is the optical depth at velocity v , and b is the Doppler parameter. τ_0 is the line center optical depth, equal to

$$\tau_0 = \frac{\sqrt{\pi} e^2 N f \lambda_0}{m_e c b}, \quad (2)$$

where N is the column density, f is the oscillator strength, and λ_0 is the laboratory line-center wavelength. We assume for simplicity that the background light source has a uniform brightness and the absorbing medium is homogeneous, with

the same optical depth along every sightline, so the observed intensity at velocity is

$$\frac{I_v}{I_0} = 1 - C_v + C_v e^{-\tau_v}, \quad (3)$$

where I_0 is the continuum intensity, I_v is the measured intensity at velocity v , C_v is the covering fraction of the absorbing medium across the emission source, such that $0 < C_v \leq 1$ (Ganguly et al. 1999; Hamann et al. 1997a; Barlow, Hamann & Sargent 1997). It is known that actual absorbers in quasar spectra can be inhomogeneous, with a range of optical depths across the projected area of the emission source (Barlow, Hamann & Sargent 1997; de Kool, Korista & Arav 2002; Hamann et al. 2001; Hamann & Sabra 2004; Arav, Korista & de Kool 2002; Arav et al. 2005). In this situation, Equation (3) yields spatially-averaged optical depths and approximate covering fractions for material with $\tau_v \gtrsim 1$ (Hamann & Sabra 2004). Real absorbers can also have velocity-dependent C_v values that can differ between lines (Barlow & Sargent 1997; Hamann et al. 1997a; Ganguly et al. 1999; Hamann et al. 2001; Hamann & Sabra 2004). The velocity-dependent effects are not important for the narrow absorption lines in our study. Therefore, for simplicity, we assume a constant covering fraction across the line profiles, e.g., $C_v = C_0$, but the value of C_0 can differ between lines. We also note that Equation (3) applies generically to partial covering situations regardless of its origins, which might include scattered light or partial covering of the accretion-disk continuum source versus the broad emission line region (Ganguly et al. 1999; Hamann & Sabra 2004). We discuss the origins of the partial covering further in Section 4.6.

To fit the lines in the low-resolution HST spectrum and the narrow AALs (velocity widths $\lesssim 30 \text{ km s}^{-1}$) in the Keck and VLT spectra, we convolve Gaussian optical depth profile with a Gaussian kernel that represents the instrumental broadening, specifically,

$$\frac{I_v}{I_0} = \int e^{-\tau_{v'}} G(v - v') dv', \quad (4)$$

where $G(v)$ is Gaussian kernel defined by

$$G(v) = \frac{1}{\sqrt{\pi} \Delta v_{ins}} e^{-\frac{\Delta v^2}{\Delta v_{ins}^2}}, \quad (5)$$

and Δv_{ins} is the instrumental velocity resolution.

We derive estimates of τ_0 and C_0 from Equation (3) by fitting the lines in doublets and multiplets simultaneously with fixed optical depth ratios determined by atomic physics. The lines are also required to have the same redshift, Doppler parameter, column density, and covering fraction. However, the tradeoff between τ_0 and C_0 in the measured line depths can lead to ambiguous results in limiting cases where $\tau_0 \gg 1$ or $\tau_0 \ll 1$, and where only a single line is available. Thus we consider four cases: 1) Heavily saturated lines based on the $\sim 1:1$ observed depth ratio of the doublet and/or flat-bottom profiles that do not reach zero intensity, see for example components 2, 7 and 11 of C IV $\lambda 1548, 1551$ and component 2 of Ly α in Figure 2. In these situations, Equation (3) simplifies to $C_0 \approx 1 - I_v/I_0$, where the covering fraction equals the observed depth of the line, and we adopt a conservative minimum optical depth of $\tau_0 \gtrsim 3$ in the weakest doublet/multiplet component. 2) Doublets or multiplets that appear unsaturated based on intermediate line

ratios, e.g., between 2:1 and 1:1 for the doublets², such as component 2 of Si IV λ 1394, 1403 in Figure 2). In this case, we use Equations (1) and (3) to solve for both C_0 and τ_0 by fitting the doublet lines simultaneously. Some examples of these fits and the partial covering determinations are described in Section 3.3.1 below (see also Figure 7). 3) Rare weak doublets that appear to have $\tau_0 \ll 1$ based on $\sim 2:1$ strength ratios, such as components 2 of Si II λ 1260, 1527 in Figure 2. In this case, the values of τ_0 and C_0 are degenerate in Equation (3) and cannot be determined separately. Thus we adopt $C_0 = 1$ to derive conservatively small lower limits on τ_0 and the column densities. And 4) single lines that do not reach zero intensity, such as component 2 of Si III λ 1206 in Figure 2. Here again we adopt $C_0 = 1$ to derive conservatively small lower limits on the column densities. We find partial covering situations in components 2, 3, 5, 7, and 11 in Q0119–046, and component 2 in Q0334–204. For Q0119–046, we perform a detailed discussion in Section 3.3.1 below. And for Q0334–204, only component 2 in C IV shows partial covering, which is not convincing. We do not perform a further partial covering analysis on this quasar.

Another complication is line blending. If the blending is moderate between two or more components in the same transition, such that distinct components with separate minima are apparent (e.g., components 2 and 3 of C IV λ 1548, 1551 in Figure 2), we fit all of the blended components simultaneously while allowing their b values and centroids to be free parameters. If the blending is more severe, such that the observed feature forms a single line (e.g., components 1, 2 and 3 of Ly α in Figure 2), we adopt b values and centroid wavelengths determined from fits to other unblended lines of similar ionised ions in the same redshift system (if available), then fit the multiple lines in the blend simultaneously to derive their separate column densities and associated errors. Finally, if the blending involves unrelated lines (from different ion or features in the Lyman forest, e.g., component 7* of N III λ 990 in Figure 3 and component 4 of N V λ 1243 in Figure 6), we again adopt b values and centroid wavelengths determined from fits to other unblended lines of similar ionised ions in the same redshift system, and then fit the line to obtain a column density or maximum column density, depending of the severity of the blending.

Tables 2 to 6 list the derived line fit parameters and associated uncertainties. Footnotes in these tables indicate the procedure used for fitting the lines and deriving or assuming values of C_0 , τ_0 , and N , while the Notes provide additional information on blends. The line data are organized in the tables according to the redshifts, i.e., component numbers in the first column as labeled in Figures 2 to 6. The uncertainties listed for most of the parameters are 1σ errors derived from the fits, affected mainly by pixel-to-pixel noise fluctuations in the spectra. They do not consider errors in the continuum placement. For very optically thick lines based on $\sim 1:1$ doublet ratios, we can obtain only lower limits on the column densities. We derive these limits from Equation (2)

using b values from our fits with $\tau_0 \gtrsim 3$. If the saturated lines are blended with neighboring systems to make their b values uncertain (e.g., components 1, 2 and 3 of Ly α in Figure 2), we derive column density limits by combining $\tau_0 \gtrsim 3$ with b values measured from other unblended lines of similar ions in the same redshift system, as marked in the Notes in the tables.

Finally, for the quasars Q0105+061, Q0334–204 and Q2044–168, we estimate upper limits on excited-state lines not detected, such as Si II* λ 1533 and C II* λ 1336, if the corresponding resonance lines, e.g., Si II λ 1527 and C II λ 1335, are cleanly measured. We use b values and redshifts from the resonance lines to manually draw synthetic line profiles at the excited-state line positions and thereby determine $\sim 3\sigma$ upper limits on the excited-state column densities.

3.3 Q0119–046

Q0119–046 is a special case because it has a rich complex of blended AALs and additional wavelength coverage from HST that includes Lyman limit absorption and AALs measured at lower spectral resolution.

3.3.1 Absorption Lines

We identify 11 distinct AAL redshift systems in the Keck spectrum (Figure 2), but only 4 systems in the HST spectrum due to the lower resolution and blending (Figure 3). We label the components in the HST spectrum 2*, 4*, 7*, and 11* to identify them loosely with the strongest components 2, 4, 7, and 11 in the Keck spectrum. Figure 3 shows important AALs such as O VI, Ne VIII and some Lyman lines in the HST spectrum compared to C IV and N V measured in the Keck spectrum. The Keck spectra in Figure 2 show that higher-ionisation lines (such as C IV) and stronger transitions (e.g., Ly α) are broader and more blended. These lines also appear to be saturated based on $\sim 1:1$ doublet ratios and/or flat-bottomed profiles that do not reach zero intensity. The depths of these saturated line yield the covering fractions (Section 3.2).

Other lines require closer examination. Figure 7 shows a partial covering analysis for components 2 and 2* in the doublets Si IV λ 1394, 1403, O VI λ 1032, 1038 and Ne VIII λ 770, 780. Specifically, fits to the stronger short-wavelength lines in these doublets are used to predict the strength of the weaker long-wavelength lines assuming $C_0 = 1$. The predicted strengths are too weak in all cases, indicating $C_0 < 1$ with specific C_0 values listed in Tables 2 and 3. There might be some ambiguity about these results for O VI and Ne VIII because these lines are not well resolved in the HST spectrum. However, the comparisons to the well-resolved N V lines in the Keck spectrum shown in Figure 3, and the tendency throughout the Q0119–046 spectrum for higher ion AALs to be broader and smoother (Figure 2) indicates that the O VI and Ne VIII lines are reasonably resolved and *not* composed of narrow saturated features that could mimic partial covering at the HST spectral resolution. There is another possibility that the long-wavelength doublet components in O VI and Ne VIII are made stronger to mimic partial covering due to blending with unrelated absorption line the Ly α forest. However, there is no evidence for significant

² The optical depth ratios for lines sharing a common lower energy state are set by the ratio of their $f\lambda$ values, where f is the oscillator strength and λ is the line wavelength. This ratio is $\sim 2:1$ for the doublets discussed in this paper, such as C IV $\tau(1548A)/\tau(1551A)$.

Table 2. Individual absorption lines of Q0119–046 (Keck spectrum). Columns show component number, absorption redshift (z_{abs}) and the corresponding velocity shift (v) relative to the emission-line redshift, line identification and rest wavelength, observation wavelength, Doppler b parameter, logarithm of column density, covering fraction, and notes (sat=saturated line, bl=blended with neighboring systems, unbl=blended with unrelated lines (e.g., lines in the Lyman forest), w=weak line). For Ly α lines, we obtain b and $N(\text{H I})$ values from the fits of the Lyman limit and Lyman series, which is described in Section 3.3.2.

#	z_{abs} v (km s $^{-1}$)	ID	λ_{obs} (Å)	b (km s $^{-1}$)	$\log N$ (cm $^{-2}$)	C_0	Notes
1	1.9633 –20 ± 202	Si IV 1394	4130.37	15.3 ± 2.7	13.11 ± 0.06	1.0 ^b	
		Si IV 1403	4156.95	—	—	—	
2	1.9642 71 ± 202	Si III 1206	3576.41	64.3 ± 8.1	13.46 ± 0.26	1.0 ^c	unbl?
		Ly α 1216	3603.74	80.8 ± 10.3	17.68 ± 0.04	0.85 ± 0.02 ^a	bl & sat
		N V 1239	3671.96	~ 53	> 14.7	1.0 ^a	bl & sat, adopt b from Si IV
		N V 1243	3683.76	—	—	—	—
		Si II 1260	3736.07	16.2 ± 2.1	12.27 ± 0.01	1.0 ^d	w
		Si II* 1265	3749.71	16.2 ± 2.1	12.34 ± 0.01	1.0 ^d	w
		C II 1335	3955.75	18.8 ± 0.6	13.66 ± 0.03	1.0 ^c	
		C II* 1336	3959.25	18.8 ± 0.6	13.94 ± 0.02	1.0 ^c	
		Si IV 1394	4131.69	52.5 ± 1.4	14.40 ± 0.03	0.95 ± 0.02 ^b	
		Si IV 1403	4158.28	—	—	—	
		Si II 1527	4525.40	16.2 ± 2.1	12.27 ± 0.01	1.0 ^d	w
		Si II* 1533	4545.38	16.2 ± 2.1	12.34 ± 0.01	1.0 ^d	w
C IV 1548	4589.09	~ 53	> 14.6	0.91 ± 0.01 ^a	bl & sat, adopt b from Si IV		
	C IV 1551	4596.71	—	—	—	—	
3	1.9659 243 ± 202	N V 1239	3674.29	29.2 ± 1.0	14.68 ± 0.03	1.0 ^b	
		N V 1243	3686.11	—	—	—	
		C IV 1548	4591.84	24.1 ± 0.6	14.70 ± 0.10	0.93 ± 0.02 ^a	sat
		C IV 1551	4599.46	—	—	—	—
4	1.9680 456 ± 202	Ly α 1216	3608.12	42.9 ± 4.4	13.66 ± 0.05	1.0 ^c	
		Si IV 1394	4136.89	11.7 ± 1.7	13.15 ± 0.05	1.0 ^b	
		Si IV 1403	4163.52	—	—	—	
5	1.9714 800 ± 202	N V 1239	3681.00	19.0 ± 1.8	13.64 ± 0.03	1.0 ^b	
		N V 1243	3692.84	—	—	—	
		Si IV 1394	4141.64	4.2 ± 1.7	12.50 ± 0.11	1.0 ^d	w
		Si IV 1403	4168.30	—	—	—	—
		C IV 1548	4600.25	11.4 ± 0.6	14.74 ± 0.08	0.92 ± 0.03 ^b	bl
C IV 1551	4607.88	—	—	—	—		
6	1.9720 860 ± 202	Si IV 1394	4142.49	4.8 ± 1.1	12.92 ± 0.07	1.0 ^b	
		Si IV 1403	4169.15	—	—	—	
7	1.9722 881 ± 202	Ly α 1216	3613.52	66.5 ± 10.5	16.11 ± 0.40	0.91 ± 0.02 ^a	bl & sat
		N V 1239	3682.10	35.3 ± 1.3	14.47 ± 0.02	1.0 ^b	bl
		N V 1243	3693.94	—	—	—	—
		Si IV 1394	4142.85	5.3 ± 2.5	12.58 ± 0.11	1.0 ^d	w
		Si IV 1403	4169.51	—	—	—	—
		C IV 1548	4601.71	~ 5	> 13.5	0.93 ± 0.02 ^a	bl & sat, adopt b from Si IV
C IV 1551	4609.35	—	—	—	—		

^a Heavily saturated lines, whose C_0 equals the observed depth of the line.

^b Unsaturated doublets, where we solve for C_0 using Equation (3).

^c Unsaturated single lines, where we adopt $C_0 = 1$ because it is not constrained.

^d Weak doublets, where we take a conservative approach by setting $C_0 = 1$.

blending because the long-wavelength lines in both ions have redshifts and profiles as predicted from the short-wavelength lines. We conclude that significant partial covering does occur for O VI and Ne VIII, with C_0 values given in Tables 2 and 3.

3.3.2 Lyman Limit and Lyman Series

The Lyman limit in Q0119–046 provides an accurate measurement of the H I column density and another estimate of the H I covering fraction. We fit the Lyman limit absorption using Equation (3) with optical depths given by

$$\tau_\lambda = 6.63 \times 10^{-18} N(\text{H I}) \left(\frac{\lambda}{912} \right)^3, \quad (6)$$

Table 2 – *continued* Individual absorption lines of Q0119–046 (Keck spectrum)

#	z_{abs} v (km s ⁻¹)	ID	λ_{obs} (Å)	b (km s ⁻¹)	$\log N$ (cm ⁻²)	C_0	Notes
8	1.9736	C IV 1548	4603.64	14.2 ± 5.8	13.45 ± 0.13	1.0^b	
	1022 ± 202	C IV 1551	4611.28	—	—	—	
9	1.9739	C IV 1548	4604.18	5.1 ± 3.8	12.65 ± 0.29	1.0^d	w
	1053 ± 202	C IV 1551	4611.83	—	—	—	—
10	1.9742	C IV 1548	4604.71	19.6 ± 9.5	13.43 ± 0.13	1.0^b	
	1083 ± 202	C IV 1551	4612.35	—	—	—	
11	1.9749	Ly α 1216	3616.47	~ 30	> 14.1	0.91 ± 0.02^a	bl & sat, adopt b from N v
	1154 ± 202	N v 1239	3685.50	29.7 ± 2.9	13.91 ± 0.04	1.0^b	bl
		N v 1243	3697.35	—	—	—	
		C IV 1548	4605.90	~ 30	> 14.3	0.90 ± 0.08^a	sat, adopt b from N v
		C IV 1551	4613.54	—	—	—	—

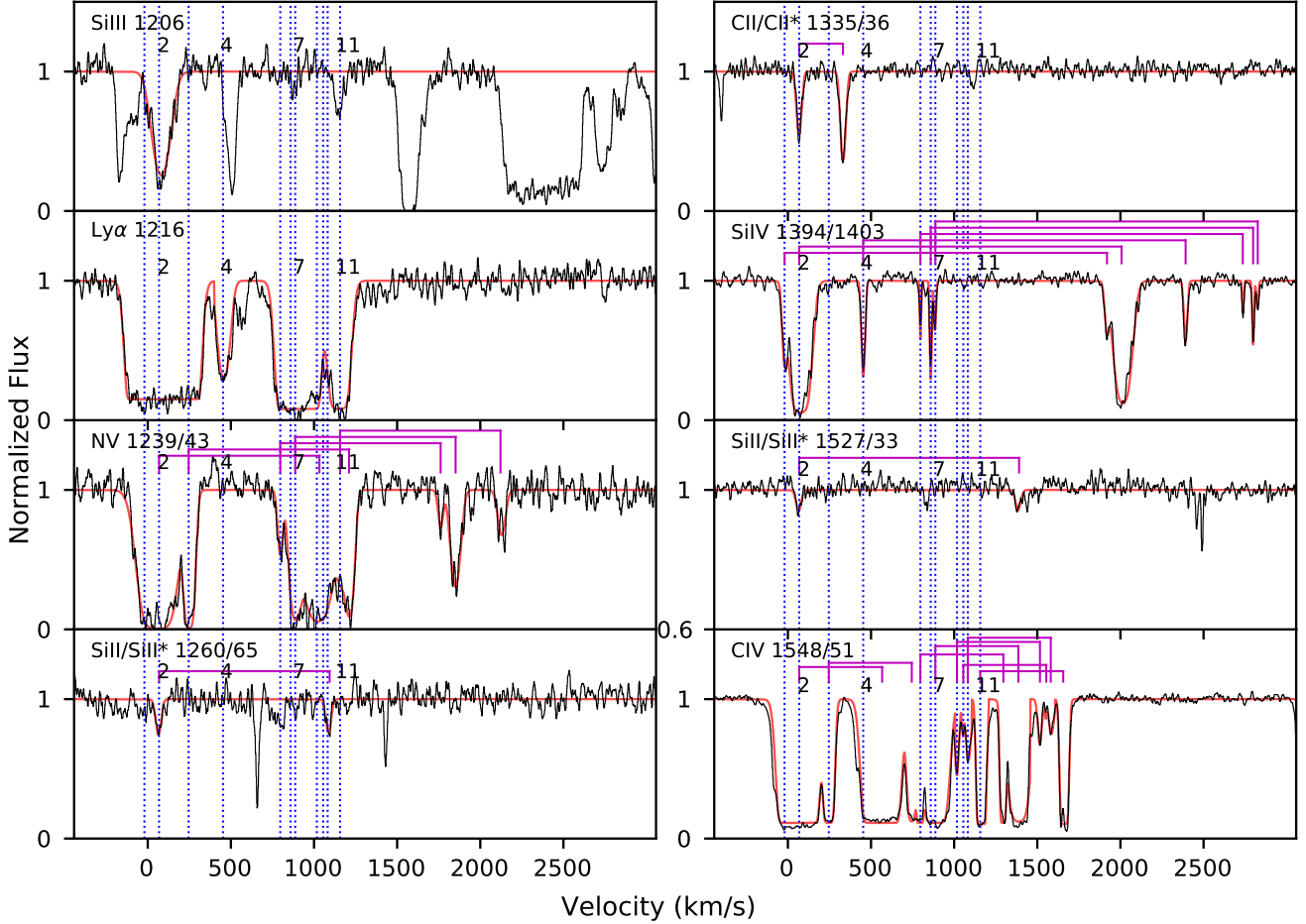


Figure 2. Q0119–046: Normalized line profiles in the Keck-HIRES spectrum plotted on a velocity scale relative to the quasar redshift (Table 1). The spectra are shown in black, and the fitting lines are shown in red. The blue dash lines are components from 1 to 11, and the brackets show the doublets. The velocities pertain to the short-wavelength lines in the doublets.

Table 3. Individual absorption lines of Q0119–046 (HST spectrum). See Table 2 for descriptions of the table contents. For the notes, nl=no obvious lines, bl=blended with neighboring systems, unbl=blended with unrelated lines (e.g., lines in the Lyman forest).

#	z_{abs} v (km s ⁻¹)	ID	λ_{obs} (Å)	b (km s ⁻¹)	$\log N$ (cm ⁻²)	C_0	Notes
2*	1.9646 111 ± 202	N IV 765	2268.60	117 ± 28	14.74 ± 0.16	1.0 ^c	
		Ne VIII 770	2284.05	147 ± 18	16.43 ± 0.38	0.68 ± 0.07 ^b	
		Ne VIII 780	2313.47	—	—	—	
		O IV 788	2335.84	110 ± 19	15.53 ± 0.14	1.0 ^c	
		L $\gamma\gamma$ 973	2883.40	80.8 ± 10.3	17.68 ± 0.04	0.92 ± 0.02 ^e	
		C III 977	2896.04	111 ± 22	14.61 ± 0.17	1.0 ^c	
		N III 990	2933.75	72.5 ± 24.1	14.08 ± 0.03	1.0 ^c	
		Ly β 1026	3040.69	80.8 ± 10.3	17.68 ± 0.04	0.92 ± 0.02 ^e	
		O VI 1032	3059.38	172 ± 41	15.92 ± 0.31	0.90 ± 0.08 ^b	
		O VI 1037	3076.33	—	—		
4*	1.9680	N IV 765	2270.53	98.9 ± 44.1	14.04 ± 0.10	1.0 ^c	bl
		O IV 788	2337.89	101.9 ± 51.0	14.86 ± 0.17	1.0 ^c	bl
		L $\gamma\gamma$ 973	2886.49	~ 43	< 14.8	1.0 ^c	unbl, adopt b from Ly α
		C III 977	2899.79	~ 100	13.33 ± 0.28	1.0 ^c	bl, adopt b from N IV
		Ly β 1026	3044.34	~ 43	< 14.8	1.0 ^c	unbl, adopt b from Ly α
7*	1.9725 911 ± 202	N IV 765	2275.25	48.9 ± 16.4	14.45 ± 0.27	1.0 ^c	
		Ne VIII 770	2290.08	~ 50	< 15.0	1.0 ^c	bl, adopt b from O VI
		Ne VIII 780	—	—	—	—	nl
		O IV 788	2334.82	~ 50	< 15.7	1.0 ^c	unbl, adopt b from N IV
		L $\gamma\gamma$ 973	2890.17	66.5 ± 10.5	16.11 ± 0.40	1.0 ^b	
		C III 977	2903.94	53.4 ± 19.3	14.34 ± 0.49	1.0 ^c	
		N III 990	2940.37	27.5 ± 11.5	< 14.5	1.0 ^c	unbl
		Ly β 1026	3048.52	66.5 ± 10.5	16.11 ± 0.40	1.0 ^b	
		O VI 1032	3067.21	49.4 ± 15.4	15.84 ± 0.39	1.0 ^b	
		O VI 1037	3084.21	—	—		
11*	1.9749 1154 ± 202	Ne VIII 770	2291.95	~ 45	< 14.4	1.0 ^c	bl, adopt b from O VI
		Ne VIII 780	—	—	—	—	nl
		L $\gamma\gamma$ 973	2893.20	~ 30	14.71 ± 0.32	1.0 ^c	bl, adopt b from Ly α
		C III 977	2906.53	~ 30	13.68 ± 0.31	1.0 ^c	bl, adopt b from Ly α
		Ly β 1026	3051.42	~ 30	14.71 ± 0.32	1.0 ^c	bl, adopt b from Ly α
		O VI 1032	3069.86	44.6 ± 12.4	15.18 ± 0.52	1.0 ^b	
		O VI 1037	3086.88	—	—		

^b Unsaturated doublets, where we solve for C_0 using Equation (3).

^c Unsaturated single lines, where we adopt $C_0 = 1$ because it is not constrained.

^e We adopt C_0 and N from fits of the Lyman limit, described in Section 3.3.2.

where $N(\text{H I})$ is the H I column density in cm⁻² (Osterbrock 1989). The main uncertainty in this analysis is the unabsorbed continuum intensity, I_0 . For this we extrapolate our best-fit power law at $\lambda > 912$ Å with $\alpha = -1.6$ (Section 2.2.1 and Figure 1) to shorter wavelengths, and we use the range of possible values from $\alpha = -1.2$ to -2.0 to assess the uncertainties. We also fix the redshift to that of component 2* (Table 3) because this system includes many strong Lyman lines and it is the only system with an H I column density large enough to produce a Lyman limit (based on our absorption-line assessments). We divide by this power law and then fit the resulting normalized continuum at $\lambda < 912$ Å using Equations (3) and (6), constrained by the median flux in narrow wavelength intervals that appear unaffected by Ly α forest lines.

The results (shown in Figure 8) indicate a covering fraction $C_0 = 0.92 \pm 0.02$ and column density $\log N(\text{H I})(\text{cm}^{-2}) = 17.68 \pm 0.04$ based our best-fit continuum with $\alpha = -1.6$. Additional fits using the full range of continua from Fig-

ure 1 ($\alpha = -1.2$ to -2.0) yield firm lower and upper limits $C_0 = 0.90$ ($\log N(\text{H I})(\text{cm}^{-2}) = 17.78$) and $C_0 = 0.95$ ($\log N(\text{H I})(\text{cm}^{-2}) = 17.60$), respectively. These covering fractions are consistent with the upper lines in the Lyman series (component 2* in Figure 3) but slightly larger than the well-determined value of $C_0 = 0.85$ for Ly α (Figure 2, Table 2). We attribute the anomaly in Ly α to its location on top of strong and broad Ly α emission line, indicating that the Ly α absorber only partially covers the broad emission-line region (see Section 4.6 for more discussion). We use a Gaussian function to model the Ly α emission line and try to eliminate its effect. But our model is only a lower limit due to the severe contamination by the strong absorptions lines. This lead to a smaller value of C_0 for Ly α .

These results for C_0 and $\log N(\text{H I})$ from the Lyman limit are more reliable than what can be determined from Lyman series lines because the lines are under-resolved in the HST spectrum and they are contaminated by the Ly α forest. Therefore, we adopt $C_0 = 0.92$ and $\log N(\text{H I})(\text{cm}^{-2}) = 17.68$

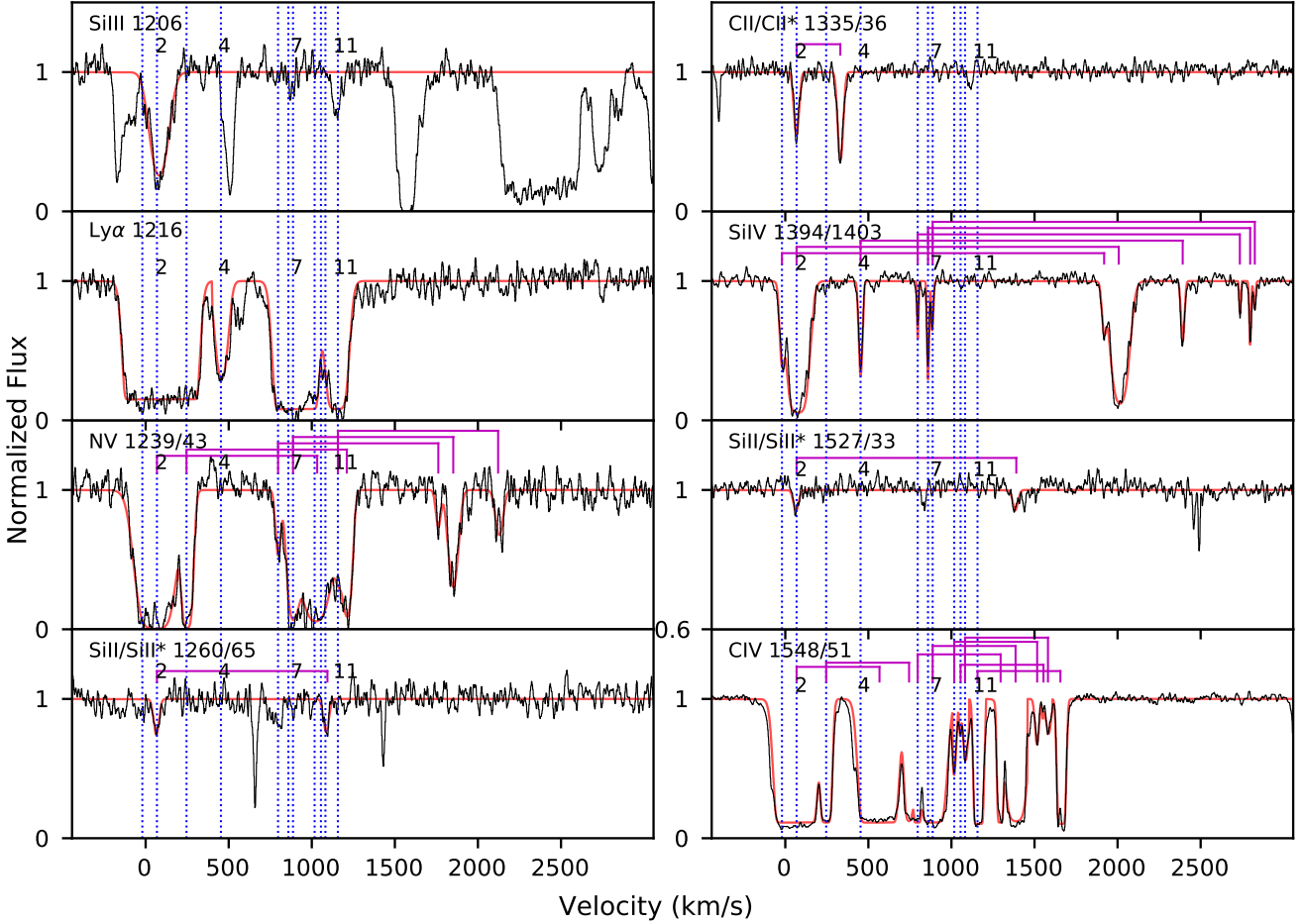


Figure 3. Q0119–046: Normalized line profiles in the HST-FOS spectrum plotted on a velocity scale relative to the quasar redshift (Table 1). The spectra are shown in black, and the fitting lines are shown in red. The blue dash lines are components, and the brackets show the doublets. The velocities pertain to the short-wavelength lines in the doublets. The bottom two panels are Ly α and NV spectra from Keck in comparison with the components of HST spectra.

and apply our fitting procedure to the upper Lyman series lines to determine that they have $b = 81 \pm 10 \text{ km s}^{-1}$ (see component 2* in Figure 3).

4 ANALYSIS

In this section, we analyze the AAL systems that have resonance lines of C II or Si II detected so that our measurements or upper limits on the corresponding excited-state lines, C II* or Si II*, provide density and location constraints on the absorption environments. This includes component 2 in Q0119–046, all components in Q0105+061, components 1, 2 and 3 in Q0334–204, and all components in Q2044–168. These AAL systems also include multiple ions of the same element, such as C II/C IV and Si II/Si III/Si IV, that we use to estimate the ionisations, total column densities, and element abundances compared to photoionisation models. Table 7 lists various derived parameters for these systems, which we discuss below.

4.1 Electron Number Density

C II and Si II have similar energy level structures with a ground $^2P^o$ term that is split into a true ground $J = 1/2$ state and a slightly excited $J = 3/2$ state. This leads to pairs of C II*/C II and Si II*/Si II lines whose ratios are density dependent because the excited $J = 3/2$ states are populated mainly by collisions from the $J = 1/2$ ground (Bahcall & Wolf 1968; Sargent, Boksenberg & Young 1982; Morris et al. 1986; Hamann et al. 2001; Dunn et al. 2010; Arav et al. 2013; Finn et al. 2014). For a simple two-level atom where the excited-state energy is small compared to kT , the density dependence can be written as

$$n_e = n_{cr} \left(\frac{N_{lo}}{N_{up}} \frac{g_{up}}{g_{lo}} - 1 \right)^{-1} \quad (7)$$

where n_e is the electron density, n_{cr} is the critical electron density of the upper state, N_{lo} and N_{up} are the column densities in the ground and excited states, respectively, and $g_{up}/g_{lo} = 2$ is the ratio of their statistical weights. For a temperature of 10^4 K , we derive $n_{cr} \approx 1766 \text{ cm}^{-3}$ for the

Table 4. Individual absorption lines of Q0105+061. See Table 2 for descriptions of the table contents. For the notes, nl=no obvious lines, sat=saturated line, bl=blended with neighboring systems, w=weak line, unbl=blended with unrelated lines (e.g., lines in the Lyman forest).

#	z_{abs} v (km s ⁻¹)	ID	λ_{obs} (Å)	b (km s ⁻¹)	$\log N$ (cm ⁻²)	C_0	Notes		
1	1.9315 -2894 ± 507	Si III 1206	3536.79	~ 5	11.90 ± 0.33	1.0 ^c	adopt b from Si II sat & bl, adopt b from Si II		
		Ly α 1216	3563.67	~ 5	> 13.3	1.0 ^a			
		Si II 1260	3694.86	5.4 ± 2.9	11.93 ± 0.38	1.0 ^c	nl		
		Si II* 1265	—	—	< 11.7	—			
		C II 1335	3912.10	5.4 ± 3.4	13.42 ± 0.23	1.0 ^c			
		C II* 1336	—	—	< 12.5	—			
		C IV 1548	4538.54	22.4 ± 5.0	14.04 ± 0.10	1.0 ^b		bl	
		C IV 1551	4546.08	—	—	—		—	
2	1.9318 -2858 ± 507	Si III 1206	3537.31	16.5 ± 1.8	14.0 ^{+1.0} _{-0.4}	1.0 ^c	sat & bl, adopt b from Si IV		
		Ly α 1216	3564.12	~ 15	> 13.8	1.0 ^a			
		N V 1239	3631.84	42.5 ± 18.6	13.77 ± 0.15	1.0 ^b	nl		
		N V 1243	3643.51	—	—	—			
		Si II 1260	3695.39	10.8 ± 0.3	14.43 ± 0.04	1.0 ^b			
		Si II* 1265	—	—	< 12.6	—			
		Si II 1304	3824.24	10.8 ± 0.3	14.43 ± 0.04	1.0 ^b			
		Si II* 1309	—	—	< 12.6	—			
		C II 1335	3912.67	18.1 ± 0.6	14.7 ^{+0.7} _{-0.2}	1.0 ^a		sat	
		C II* 1336	—	—	< 12.8	—		nl	
		Si IV 1394	4086.27	15.1 ± 0.4	14.1 ^{+0.7} _{-0.2}	1.0 ^b		nl	
		Si IV 1403	4112.70	—	—	—			
		Si II 1527	4476.10	10.8 ± 0.3	14.43 ± 0.04	1.0 ^b			
		Si II* 1533	—	—	< 12.6	—			
		C IV 1548	4538.93	~ 15	14.7 ± 0.5	1.0 ^a			bl, sat, adopt b from Si IV
		C IV 1551	4546.47	—	—	—			—
		Fe II 2374	6961.38	9.0 ± 1.0	13.55 ± 0.09	1.0 ^b			nl
		Fe II 2383	6985.73	—	—	—			
		Fe II 2587	7583.47	—	—	—			
		Mg II 2796	8198.37	15.4 ± 1.6	13.77 ± 0.07	1.0 ^b			
		Mg II 2804	8219.42	—	—	—			
Mg I 2853	8364.39	11.1 ± 3.1	12.08 ± 0.10	1.0 ^c					
3	1.9324 -2797 ± 507	Si III 1206	3537.96	4.3 ± 2.2	11.87 ± 0.15	1.0 ^c	sat & bl, adopt b from Mg II		
		Ly α 1216	3564.84	~ 6	> 13.4	1.0 ^a			
		Si II 1260	3696.06	4.6 ± 0.5	12.68 ± 0.02	1.0 ^b	nl		
		Si II* 1265	—	—	< 12.7	—			
		Si II 1304	3824.94	4.6 ± 0.5	12.68 ± 0.02	1.0 ^b			
		Si II* 1309	—	—	< 12.7	—			
		C II 1335	3913.38	5.0 ± 0.2	13.64 ± 0.03	1.0 ^c			
		C II* 1336	—	—	< 12.3	—		nl	
		Si II 1527	4476.91	4.6 ± 0.5	12.68 ± 0.02	1.0 ^b		nl	
		Si II* 1533	—	—	< 12.7	—			
		C IV 1548	4539.95	6.8 ± 3.8	12.66 ± 0.18	1.0 ^d			w
		C IV 1551	4547.48	—	—	—			—
		Mg II 2796	8199.99	5.7 ± 0.7	12.63 ± 0.03	1.0 ^b			w
		Mg II 2804	8221.04	—	—	—			
Mg I 2853	8366.08	3.5 ± 4.0	10.67 ± 0.49	1.0 ^c	w				

^a Heavily saturated lines, whose C_0 equals the observed depth of the line.^b Unsaturated doublets, where we solve for C_0 using Equation (3).^c Unsaturated single lines, where we adopt $C_0 = 1$ because it is not constrained.^d Weak doublets, where we take a conservative approach by setting $C_0 = 1$.

Si II upper state and $n_{cr} \approx 49$ cm⁻³ for C II (using collision strengths from Tayal (2008a,b) and radiative decay rates from the NIST atomic spectra database³).

Table 7 shows the electron densities in Si II or C II regions that result from Equation (7) combined with the column density data in Tables 2 to 6. The excited-state lines are detected only in component 2 of Q0119–046. The density listed for Q0119–046 derives from the $N(\text{Si II}^*)/N(\text{Si II})$ with the result $\log n_e$ (cm⁻³) = 3.4 ± 0.3. This is consistent with the

³ <http://www.nist.gov/pml/data/asd.cfm>

Table 4 – *continued* Individual absorption lines of Q0105+061

#	z_{abs} v (km s ⁻¹)	ID	λ_{obs} (Å)	b (km s ⁻¹)	$\log N$ (cm ⁻²)	C_0	Notes
4	1.9345 -2590 ± 507	Si III 1206	3540.47	5.7 ± 3.8	12.11 ± 0.30	1.0 ^c	
		Ly α 1216	3567.31	~ 6	> 13.4	1.0 ^a	sat & bl, adopt b from Si II
		Si II 1260	3698.66	5.7 ± 1.3	11.72 ± 0.49	1.0 ^c	
		Si II* 1265	—	—	< 11.5	—	nl
		C II 1335	3916.10	10.1 ± 1.2	12.98 ± 0.05	1.0 ^c	
		C II* 1336	—	—	< 12.5	—	nl
		Si IV 1394	4089.98	4.8 ± 2.3	11.61 ± 0.71	1.0 ^d	w
		Si IV 1403	4116.42	—	—	—	—
		C IV 1548	4543.11	9.0 ± 3.1	13.03 ± 0.14	1.0 ^b	
C IV 1551	4550.64	—	—	—	—		
5	1.9349 -2544 ± 507	Si III 1206	3541.02	~ 12	> 13.1	1.0 ^a	sat & bl, adopt b from Si II
		Ly α 1216	3567.88	~ 11	> 13.6	1.0	sat & bl, adopt b from Mg II
		Si II 1260	3699.25	12.0 ± 0.8	12.77 ± 0.05	1.0 ^b	
		Si II* 1265	—	—	< 12.0	—	nl
		Si II 1304	3828.24	12.0 ± 0.8	12.77 ± 0.05	1.0 ^b	
		Si II* 1309	—	—	< 12.0	—	nl
		C II 1335	3916.75	11.4 ± 0.4	13.82 ± 0.02	1.0 ^c	
		C II* 1336	—	—	< 12.3	—	nl
		Si IV 1394	4090.46	7.1 ± 0.5	13.45 ± 0.05	1.0 ^b	
		Si IV 1403	4116.92	—	—	—	—
		Si II 1527	4480.78	12.0 ± 0.8	12.77 ± 0.05	1.0 ^b	
		Si II* 1533	—	—	< 12.0	—	nl
		C IV 1548	4543.73	~ 7	> 13.7	1.0 ^a	sat & bl, adopt b from Si IV
		C IV 1551	4551.27	—	—	—	—
		Mg II 2796	8207.05	10.6 ± 0.9	12.85 ± 0.1	1.0 ^c	
Mg II 2804	8228.12	—	—	—	unbl		
6	1.9353 -2503 ± 507	Si III 1206	3541.57	~ 20	> 13.3	1.0 ^a	sat & bl, adopt b from Si II
		Ly α 1216	3568.41	~ 21	> 14.0	1.0 ^a	sat & bl, adopt b from Mg II
		N V 1239	3636.32	32.5 ± 12.5	13.36 ± 0.06	1.0 ^b	
		N V 1243	3648.01	—	—	—	—
		Si II 1260	3699.83	19.7 ± 0.6	13.46 ± 0.02	1.0 ^b	
		Si II* 1265	—	—	< 12.5	—	nl
		Si II 1304	3828.84	19.7 ± 0.6	13.46 ± 0.02	1.0 ^b	
		Si II* 1309	—	—	< 12.5	—	nl
		C II 1335	3917.41	20.6 ± 0.5	14.41 ± 0.02	1.0 ^c	
		C II 1336	—	—	< 12.3	—	nl
		Si IV 1394	4091.07	25.2 ± 5.4	14.0 ^{+0.7} _{-0.2}	1.0 ^b	
		Si IV 1403	4117.53	—	—	—	—
		Si II 1527	4481.49	19.7 ± 0.6	13.46 ± 0.02	1.0 ^b	
		Si II* 1533	—	—	< 12.5	—	nl
		C IV 1548	4544.40	~ 25	> 14.2	1.0 ^a	sat & bl, adopt b from Si IV
		C IV 1551	4551.94	—	—	—	—
Mg II 2796	8208.39	20.8 ± 1.1	13.31 ± 0.03	1.0 ^b			
Mg II 2804	8229.47	—	—	—	—		

observed ratio of $N(\text{C II}^*)/N(\text{C II})$ near 2, which yields only a lower limit $\log n_e$ (cm⁻³) $\gtrsim 2.2$ (consistent with [Sargent, Boksenberg & Young 1982](#)).

All of the other quasars with non-detections provide only upper limits on the densities. The upper limits listed for components 2, 3, 5 and 6 in Q0105+061 are based on $N(\text{Si II}^*)/N(\text{Si II})$ because we fit multiple Si II lines (1260, 1304, and 1527 Å) simultaneously with the same b parameter, velocity shift and column density, which lead to reasonably good constraints. The upper limits listed for components 1 and 4 in Q0105+061 are based on $N(\text{C II}^*)/N(\text{C II})$ because Si II lines are weak and only Si II $\lambda 1260$ is detected. The densities listed for Q0334–204 and Q2044–168 derive

from $N(\text{C II}^*)/N(\text{C II})$ because the resonance C II $\lambda 1335$ lines are well measured and this ratio provides smaller upper limits than $N(\text{Si II}^*)/N(\text{Si II})$. The upper limits in these quasars range from $\lesssim 150$ to $\lesssim 15$ cm⁻³.

4.2 Photoionisation Models

We assume that the absorbers are in photoionisation equilibrium with the quasar radiation field and examine their ionisation properties using the computer code CLOUDY (version 13.03, [Ferland et al. 2013](#)). The calculations use a plane-parallel absorbing geometry, solar abundances, and a constant gas density $n_{\text{H}} = 100$ cm⁻³. The specific value of the

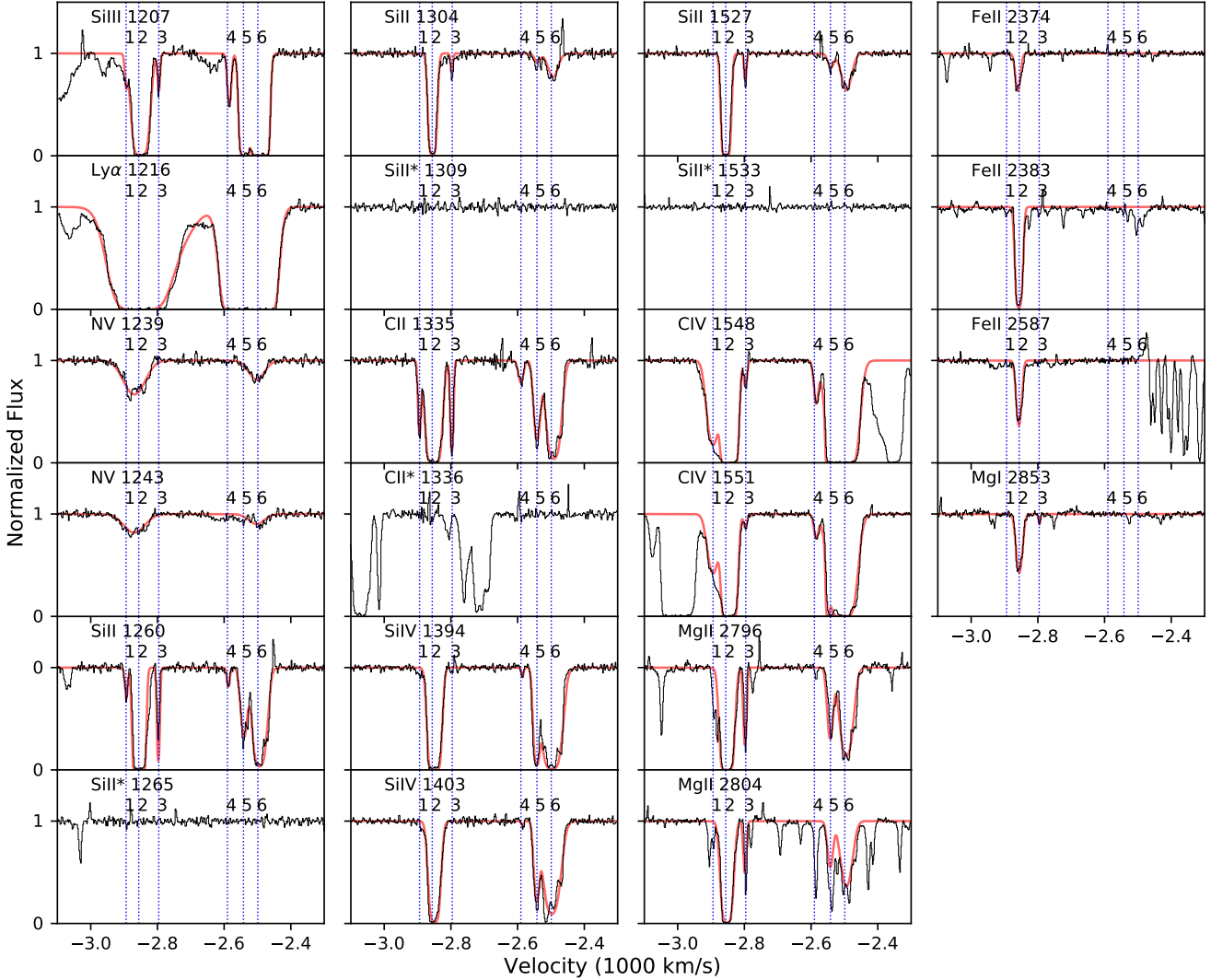


Figure 4. Q0105+061: Normalized line profiles in the VLT-UVES spectrum plotted on a velocity scale relative to the quasar redshift (Table 1). The spectra are shown in black, and the fitting lines are shown in red. The blue dash lines are components.

density is not important for our analysis of the ground-state column densities (Hamann 1997; Hamann et al. 2002; Leighly, Dietrich & Barber 2011). Recent work by Baskin, Laor & Stern (2014) favors constant pressure absorbing clouds instead of constant density for broad absorption line outflows. However, experiments with CLOUDY show that this also does not have an impact on our results. The ionisation structure does depend on the shape and intensity of the incident spectral energy distribution (SED). We use an SED that is roughly characteristic of luminous quasars (Reeves & Turner 2000; Richards et al. 2006; Hopkins, Richards & Hernquist 2007; Shull, Stevans & Danforth 2012). It is described by a power law, $f_\nu \propto \nu^\alpha$, with spectral indices $\alpha_{UV} = -0.5$ and $\alpha_X = -0.9$ at UV and X-ray wavelengths, respectively. These segments are normalized to yield the two-point power law index $\alpha_{OX} = -1.7$ between 2500 Å and 2

keV (Hamann et al. 2013). The UV and X-ray segments connect smoothly using a Planck exponential with temperature 350,000 K. We specify the intensity of this radiation field using the ionisation parameter, U , which is defined as the dimensionless ratio between the number density of hydrogen-ionising photons at the illuminated face of the clouds to the number density of hydrogen atoms, e.g.,

$$U \equiv \frac{\Phi(\text{H})}{n_{\text{H}}c}, \quad (8)$$

where n_{H} is the total hydrogen density, c is the speed of light, and $\Phi(\text{H})$ is the flux of H-ionising photons given by

$$\Phi(\text{H}) = \frac{1}{4\pi R^2} \int_{\nu_1}^{\infty} \frac{L_\nu}{h\nu} d\nu, \quad (9)$$

Table 5. Individual absorption lines of Q0334–204. See Table 2 for descriptions of the table contents. For the notes, nl=no obvious lines, bl=blended with neighboring systems, sat=saturated line, w=weak line. For $N(\text{H I})$ lower limit estimates, we adopt b from C IV, and assume $\tau_0 > 3$ in Ly δ 950 Å. We use Ly δ because Ly δ has smaller oscillator strength than Ly α , Ly β and Ly γ , which results in more accurate estimation of the lower limit.

#	z_{abs} v (km s ⁻¹)	ID	λ_{obs} (Å)	b (km s ⁻¹)	$\log N$ (cm ⁻²)	C_0	Notes
1	3.0902 -3035 ± 94	Ly δ 950	3884.64	~ 11	> 15.2	1.0 ^a	sat & bl, adopt b from C IV
		Ly γ 973	3977.87	—	—	—	—
		Ly β 1026	4195.35	—	—	—	—
		Ly α 1216	4972.28	—	—	—	—
		O VI 1032	4220.86	~ 11	13.86 ± 1.12	1.0 ^b	bl, adopt b from C IV
		O VI 1038	4244.14	—	—	—	—
		Si III 1206	4934.83	10.1 ± 0.7	13.02 ± 0.04	1.0 ^c	—
		Si II 1260	5155.33	5.1 ± 2.5	11.84 ± 0.22	1.0 ^c	—
		Si II* 1265	—	—	< 11.2	—	nl
		C II 1335	5458.43	6.3 ± 5.5	12.91 ± 0.14	1.0 ^c	—
		C II* 1336	—	—	< 12.4	—	nl
		Si IV 1394	5700.66	6.8 ± 0.3	13.32 ± 0.02	1.0 ^b	—
		Si IV 1403	5737.54	—	—	—	—
		C IV 1548	6332.35	10.6 ± 0.9	13.96 ± 0.06	1.0 ^b	—
		C IV 1551	6342.86	—	—	—	—
2	3.0906 -3006 ± 94	Ly δ 950	3885.02	~ 16	> 15.4	1.0 ^a	sat & bl, adopt b from C IV
		Ly γ 973	3978.26	—	—	—	—
		Ly β 1026	4195.79	—	—	—	—
		Ly α 1216	4972.92	—	—	—	—
		O VI 1032	4221.17	~ 16	14.05 ± 1.34	1.0 ^b	bl, adopt b from C IV
		O VI 1038	4244.45	—	—	—	—
		Si III 1206	4935.32	9.0 ± 0.9	12.92 ± 0.06	1.0 ^c	—
		Si II 1260	5155.95	5.7 ± 1.5	11.95 ± 1.33	1.0 ^c	—
		Si II* 1265	—	—	< 11.2	—	nl
		C II 1335	5459.11	3.6 ± 11.5	12.65 ± 0.33	1.0 ^c	—
		C II* 1336	—	—	< 11.9	—	nl
		Si IV 1394	5701.29	5.8 ± 1.4	12.96 ± 0.20	1.0 ^b	—
		Si IV 1403	5738.17	—	—	—	—
		C IV 1548	6333.09	15.8 ± 1.3	14.4 ^{+0.4} _{-0.3}	0.75 ± 0.01 ^b	bl
		C IV 1551	6343.60	—	—	—	—
3	3.0908 -2991 ± 94	Ly δ 950	3885.21	~ 9	> 15.1	1.0 ^a	sat & bl, adopt b from C IV
		Ly γ 973	3978.45	—	—	—	—
		Ly β 1026	4196.06	—	—	—	—
		Ly α 1216	4973.26	—	—	—	—
		O VI 1032	4221.53	~ 9	13.83 ± 1.74	1.0 ^b	bl, adopt b from C IV
		O VI 1038	4244.80	—	—	—	—
		Si III 1206	4935.49	7.2 ± 1.3	12.86 ± 0.25	1.0 ^c	—
		Si II 1260	5156.14	2.1 ± 1.2	11.47 ± 1.03	1.0 ^c	—
		Si II* 1265	—	—	< 10.9	—	nl
		C II 1335	5459.30	6.4 ± 8.1	13.04 ± 0.04	1.0 ^c	—
		C II* 1336	—	—	< 12.4	—	nl
		Si IV 1394	5701.58	5.0 ± 0.5	12.94 ± 0.03	1.0 ^b	—
		Si IV 1403	5738.46	—	—	—	—
		C IV 1548	6333.60	9.1 ± 1.3	13.48 ± 0.06	1.0 ^b	—
		C IV 1551	6344.11	—	—	—	—

^a Heavily saturated lines, whose C_0 equals the observed depth of the line.

^b Unsaturated doublets, where we solve for C_0 using Equation (3).

^c Unsaturated single lines, where we adopt $C_0 = 1$ because it is not constrained.

^d Weak doublets, where we take a conservative approach by setting $C_0 = 1$.

where L_ν is the quasar luminosity density, R is the radial distance between the absorber and the quasar, and $h\nu_1 = 13.6$ eV.

We run the CLOUDY simulations with a fixed H I column density $\log N(\text{H I})(\text{cm}^{-2}) = 17.7$ and a total column

density $\log N(\text{H})(\text{cm}^{-2}) = 20.9$ for Q0119–046 based on our measurements in Section 3.3.2 (Tables 2 and 3) and Section 4.3 below. For the other three quasars, we adopt $\log N(\text{H I})(\text{cm}^{-2}) = 16$ consistent with the lower limits listed in Tables 4 to 6. We adopt $\log N(\text{H I})(\text{cm}^{-2}) = 16$ to illustrate

Table 5 – *continued* Individual absorption lines of Q0334–204

#	z_{abs} v (km s ⁻¹)	ID	λ_{obs} (Å)	b (km s ⁻¹)	$\log N$ (cm ⁻²)	C_0	Notes
4	3.0911 -2970 ± 94	Ly δ 950	3885.49	~ 8	> 15.1	1.0 ^a	sat & bl, adopt b from C IV
		Ly γ 973	3978.75	—	—	—	—
		Ly β 1026	4196.28	—	—	—	—
		Ly α 1216	4973.36	—	—	—	—
		O VI 1032	4221.70	~ 8	13.13 ± 1.21	1.0 ^b	bl, adopt b from C IV
		O VI 1038	4244.98	—	—	—	—
		Si III 1206	4935.89	10.1 ± 2.9	12.77 ± 0.07	1.0 ^c	—
		Si IV 1394	5701.96	6.9 ± 9.9	12.50 ± 2.00	1.0 ^d	w
		Si IV 1403	5738.82	—	—	—	—
		C IV 1548	6333.75	7.8 ± 0.8	13.18 ± 0.04	1.0 ^b	bl
C IV 1551	6344.27	—	—	—	—		
5	3.0914 -2948 ± 94	Ly δ 950	3885.78	~ 14	> 15.3	1.0 ^a	sat & bl, adopt b from C IV
		Ly γ 973	3979.04	—	—	—	—
		Ly β 1026	4196.88	—	—	—	—
		Ly α 1216	4973.87	—	—	—	—
		O VI 1032	4222.11	17.7 ± 16.6	13.89 ± 1.92	1.0 ^b	—
		O VI 1038	4245.39	—	—	—	—
		Si III 1206	4936.39	11.6 ± 0.8	12.90 ± 0.04	1.0 ^c	—
		C IV 1548	6334.35	13.6 ± 1.4	13.28 ± 0.03	1.0 ^b	—
		C IV 1551	6344.87	—	—	—	—
		6	3.0924 -2875 ± 94	Ly δ 950	3886.73	10.5 ± 3.7	13.10 ± 1.05
Ly γ 973	3980.01			—	—	—	—
Ly β 1026	4197.72			—	—	—	—
Ly α 1216	4973.87			—	—	—	—
O VI 1032	4223.14			15.7 ± 3.5	14.19 ± 0.56	1.0 ^b	—
O VI 1038	4246.42			—	—	—	—
C IV 1548	6335.83			11.0 ± 0.7	13.40 ± 0.02	1.0 ^b	—
C IV 1551	6346.35			—	—	—	—

the results in a regime where the clouds are optically thin in the Lyman continuum such that the calculated ionisations do not depend on the specific value of $N(\text{H I})$. The actual H I column densities are not known for these quasars. We discuss other possibilities in Section 4.3 below.

4.3 Ionisation & Total Column Densities

Figures 9 to 12 show predicted ionisation fractions for the well-measured AAL systems we discuss below. These predictions compared to the measured column density ratios in various ion pairs (C II/C IV, Si II/Si IV, Si II/Si III, etc.) yield estimates of the ionisation parameter U (shown by vertical lines in the figures) and its uncertainties (horizontal bars, based on the column density uncertainties in Tables 2 to 6). If the column density ratios of similar ion pairs (e.g. C II/C IV and Si II/Si IV) are consistent with a single U value, we derive a weighted mean U and weighted error. The results are listed in Table 7.

The temperature is the most important parameter in the far-UV. We ran additional CLOUDY models with the temperatures 175,000 K and 700,000 K, which might be considered extreme ($\pm 3\sigma$) deviations from the continuum we adopted (Section 4.2). Generally, we found the ionisation parameter $\log U$ in the models changed by $\lesssim 0.1$ if considering 1σ deviation, which is less than or similar to other uncertainties in the measured values of $\log U$.

Many of the systems in our sample exhibit a range of

ions, e.g., from Mg I, Si II, C II, and Mg II up to N V, O VI, and Ne VIII, that cannot coexist spatially in the same absorber. In principle, these observed lines could form in the same clouds at a single U if the column densities are large enough to radiatively shield the lower ions behind a thick layer of ionised gas. However, in component 2 of Q0119–046, the amount of shielding is well constrained by our measurement of $N(\text{H I})$, e.g., the Lyman limit shown in Figures 1 and 8. Our CLOUDY simulations show that this produces minimal shielding with minimal effects on the ionisation structure. Therefore, a range in U is required.

The two U values listed for Q0119–046 in Table 7 illustrate the range. They derive from the column density ratio Si II/Si III, which yields $\log U \sim -1.9$, up to O VI/Ne VIII, which yields $\log U \sim 0.9$ (assuming solar O/Ne abundances, see Figure 9). If the Ne VIII absorber is at the same distance from the quasar as the low-ionisation Si II-absorbing region, then the range in U values implies that the Ne VIII gas is ~ 630 times less dense than the Si II region (i.e., $n_e \sim 4 \text{ cm}^{-3}$ compared to $\sim 2500 \text{ cm}^{-3}$ for Si II).

It is necessary to note that there is a large difference in the Doppler b parameters between Si III ($b \sim 64 \text{ km s}^{-1}$) and Si II ($b \sim 16 \text{ km s}^{-1}$). The large difference indicates that the lines sample different physical regions in the absorber or, perhaps, that the Si III line is blended with a feature in the Ly α forest. We note that the Si III line width is similar to Si IV and, therefore, it seems likely that Si III is broader

Table 6. Individual absorption lines of Q2044–168. See Table 2 for descriptions of the table contents. For the notes, nl=no obvious lines, sat=saturated line, bl=blended with neighboring systems, unbl=blended with unrelated lines (e.g., lines in the Lyman forest).

#	z_{abs} v (km s ⁻¹)	ID	λ_{obs} (Å)	b (km s ⁻¹)	$\log N$ (cm ⁻²)	C_0	Notes
1	1.9183 -2113 ± 102	Si III 1206	3520.94	8.6 ± 0.7	12.51 ± 0.03	1.0 ^c	
		Lyα 1216	3547.58	~ 17	> 13.8	1.0 ^a	sat & bl, adopt b from C IV
		C II 1335	3894.54	10.2 ± 4.4	13.0 ^{+0.1} _{-0.5}	1.0 ^c	
		C II* 1336	—	—	< 12.7	—	nl
		Si IV 1394	4067.42	13.6 ± 0.6	12.89 ± 0.01	1.0 ^b	
		Si IV 1403	4093.71	—	—	—	
		C IV 1548	4518.09	16.5 ± 0.6	14.35 ± 0.04	1.0 ^b	
		C IV 1551	4525.59	—	—	—	
2	1.9190 -2042 ± 102	Si III 1206	3521.77	9.0 ± 0.5	13.01 ± 0.04	1.0 ^c	
		Lyα 1216	3548.51	~ 16	> 13.8	1.0 ^a	sat & bl, adopt b from C IV
		N V 1239	3616.07	12.2 ± 1.7	13.54 ± 0.06	1.0 ^b	
		N V 1243	3627.70	—	—	—	
		Si II 1260	3679.17	8.5 ± 8.1	12.26 ± 0.27	1.0 ^c	
		Si II* 1265	—	—	< 11.2	—	nl
		C II 1335	3895.49	8.2 ± 0.4	13.45 ± 0.02	1.0 ^c	
		C II* 1336	—	—	< 12.3	—	nl
		Si IV 1394	4068.34	9.0 ± 0.3	13.34 ± 0.02	1.0 ^b	
		Si IV 1403	4094.66	—	—	—	
		C IV 1548	4519.15	15.8 ± 0.7	14.44 ± 0.04	1.0 ^b	
		C IV 1551	4526.65	—	—	—	
		Mg II 2796	8162.36	15.2 ± 5.9	< 12.49	1.0 ^b	unbl
Mg II 2804	8183.31	—	—	—	—		
3	1.9198 -1960 ± 102	Si III 1206	3522.76	21.5 ± 1.0	13.10 ± 0.04	1.0 ^c	bl
		Lyα 1216	3549.45	~ 8	> 13.5	1.0 ^a	sat & bl, adopt b from C IV
		C II 1335	3896.55	8.5 ± 1.7	12.76 ± 0.01	1.0 ^c	
		C II* 1336	—	—	< 12.1	—	nl
		Si IV 1394	4069.43	5.0 ± 0.7	12.22 ± 0.03	1.0 ^b	
		Si IV 1403	4095.75	—	—	—	
		C IV 1548	4520.42	8.1 ± 5.7	13.33 ± 0.04	1.0 ^b	
		C IV 1551	4527.92	—	—	—	
4	1.9201 -1929 ± 102	Si III 1206	3523.11	18.0 ± 1.1	12.89 ± 0.03	1.0 ^c	bl
		Lyα 1216	3549.87	~ 11	> 13.6	1.0 ^a	sat & bl, adopt b from C IV
		N V 1239	3617.50	9.1 ± 7.0	13.15 ± 0.13	1.0 ^c	
		N V 1243	3629.12	—	—	—	unbl
		C II 1335	3896.97	8.5 ± 0.6	13.27 ± 0.03	1.0 ^c	
		C II* 1336	—	—	< 12.3	—	nl
		Si IV 1394	4069.89	7.0 ± 0.4	12.70 ± 0.02	1.0 ^b	
		Si IV 1403	4096.22	—	—	—	
		C IV 1548	4520.89	10.7 ± 0.6	14.19 ± 0.05	1.0 ^b	
		C IV 1551	4528.40	—	—	—	
5	1.9206 -1878 ± 102	Si III 1206	3523.66	9.0 ± 0.9	12.30 ± 0.04	1.0 ^c	
		Lyα 1216	3550.44	~ 11	> 13.6	1.0 ^a	sat & bl, adopt b from C IV
		C II 1335	3897.59	14.8 ± 2.1	13.0 ^{+0.2} _{-0.3}	1.0 ^c	
		C II* 1336	—	—	< 12.5	—	nl
		Si IV 1394	4070.56	6.7 ± 0.6	12.39 ± 0.05	1.0 ^b	
		Si IV 1403	4096.89	—	—	—	
		C IV 1548	4521.65	10.6 ± 0.5	13.78 ± 0.04	1.0 ^b	
		C IV 1551	4529.16	—	—	—	

^a Heavily saturated lines, whose C_0 equals the observed depth of the line.

^b Unsaturated doublets, where we solve for C_0 using Equation (3).

^c Unsaturated single lines, where we adopt $C_0 = 1$ because it is not constrained.

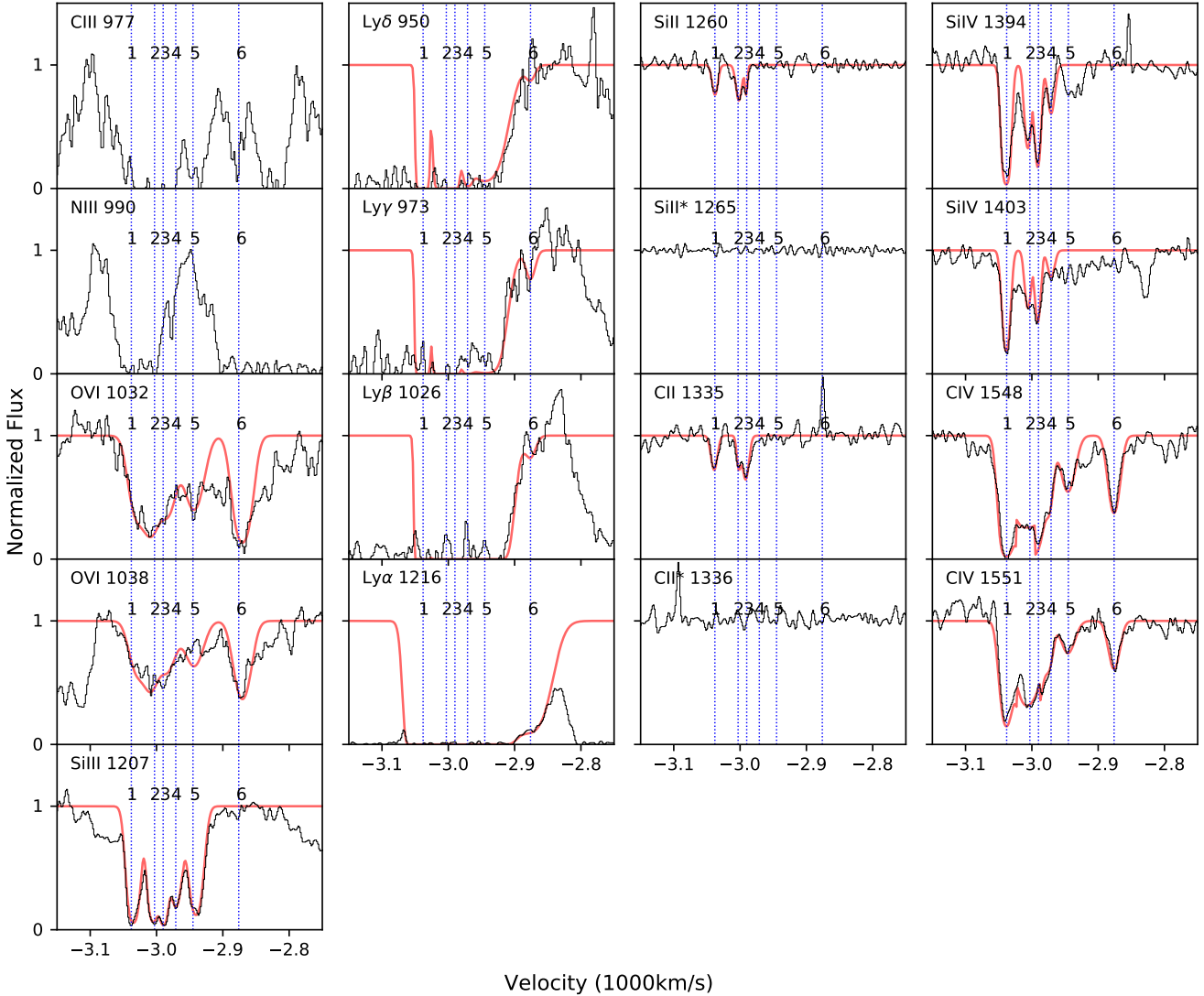


Figure 5. Q0334–204: Normalized line profiles in the VLT-UVES spectrum plotted on a velocity scale relative to the quasar redshift (Table 1). The spectra are shown in black, and the fitting lines are shown in red. The blue dash lines are components.

than Si II because it has contributions from regions of higher ionization.

We apply the same procedure to derive U values and ranges for the other quasars, again assuming solar abundance ratio if ion pairs in the same elements are not available. Table 7 lists the U values and the ions used for each component.

To estimate the total hydrogen column densities, we assume that the measured H I column densities reside primarily with the lower metal ions (see Section 4.5 for more discussion). For example, for component 2 in Q0119–046, we apply an ionisation correction $H\text{I}/H \approx -3.2$ based on $\log U \sim -1.9$ from Si II/Si III to the observed $N(\text{H I})$ value to derive a total column density of $\log N(\text{H}) \text{ (cm}^{-2}\text{)} = 20.9$ in this absorber. For the other quasars with only conservative

lower limits on $N(\text{H I})$, we derive conservative lower limits on $N(\text{H})$. These results are also listed in Table 7.

It is important to note that the results for U and $N(\text{H})$ for the other quasars, with only lower limits on $N(\text{H I})$, are based on CLOUDY models where the absorber is optically thin in the ionising continuum (Section 4.2). If shielding does play a role, then the total column densities would need to be at least as large as Q0119–046, where $\log U \sim -1.9$ and $\log N(\text{H}) \text{ (cm}^{-2}\text{)} = 20.9$ combined to produce significant absorption at the H I Lyman edge. We cannot exclude this possibility for the other quasars, but their absorbers are clearly different from Q0119–046 given their lower densities and larger distances (discussed below).

Another constraint on the ionisation and densities comes from the neutral Mg I $\lambda 2853$ line that appears uniquely in components 2 and 3 of Q0105+061. This ion can-

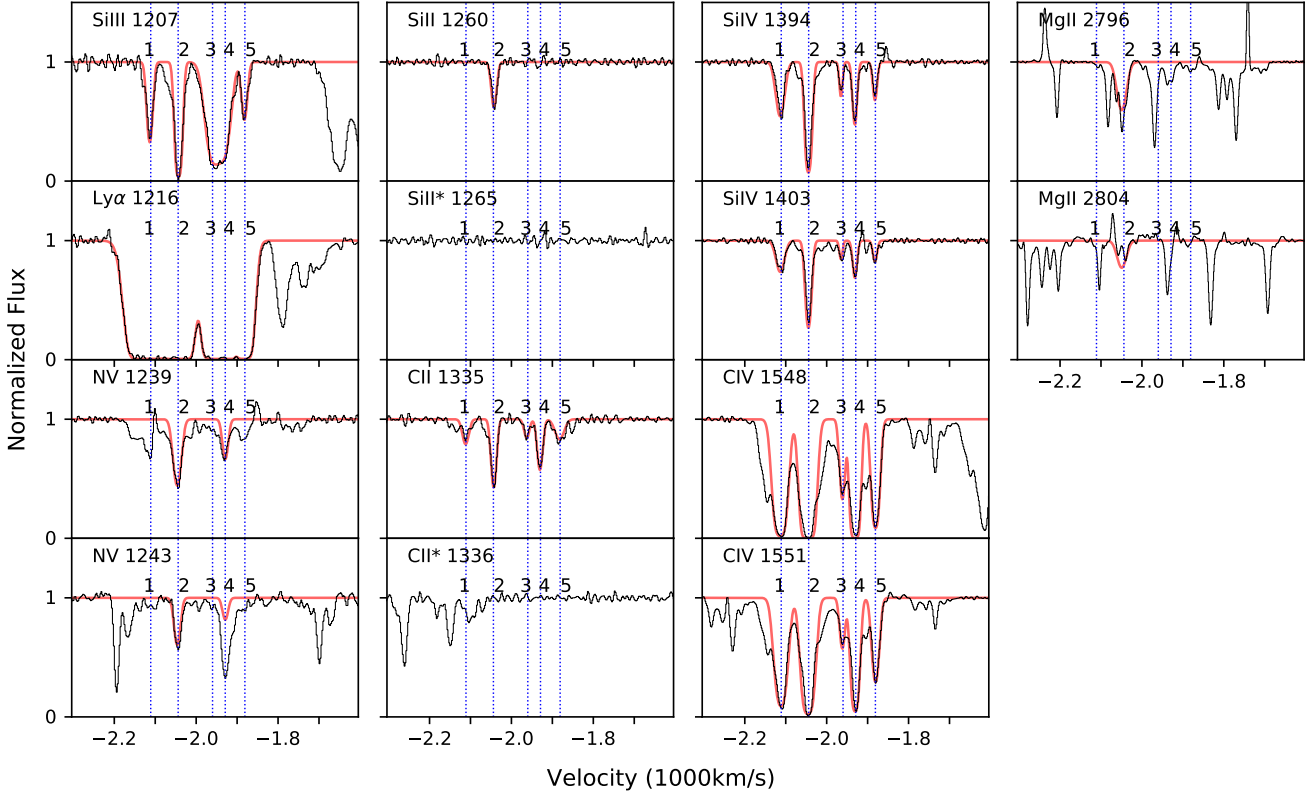


Figure 6. Q2044–168: Normalized line profiles in the VLT-UVES spectrum plotted on a velocity scale relative to the quasar redshift (Table 1). The spectra are shown in black, and the fitting lines are shown in red. The blue dash lines are components.

not be shielded behind an H II–H I recombination front because its ionisation potential 7.65 eV is well below that of H I at 13.6 eV. Therefore, the Mg I lines suggest that high densities lead to very low ionisation parameters in some portions of these absorbers. Our CLOUDY simulations (Figure 10) indicate that significant amounts of Mg I require $\log U < -5$. (The results are the same if we use larger column densities like Q0119–046 because the shielding effects for Mg I are still negligible.) For component 2 in Q0105+061 with estimated $\log U \approx -3.0$ in the Si II region (top panel of Figure 10), we estimated an upper limit on the density of $n_e \lesssim 7 \text{ cm}^{-3}$ (Table 7). If the Mg I line forms at the same radial distance as Si II, then there would need to be regions with densities $\gtrsim 100$ times larger than the Si II gas to support measurable Mg I.

4.4 Radial Distance

Here we estimate the radial distance, R , of the Si II or C II AAL regions from the quasars using n_e and U in the Si II or C II regions derived in Sections 4.1 and 4.3, respectively. First we combine our adopted quasar spectrum from Section 4.2 with Equation (8) and Equation (9) to derive an

expression for the distance,

$$R = 40.8 \left(\frac{\nu L_\nu(1500\text{\AA})}{10^{46} \text{ ergs/s}} \right)^{\frac{1}{2}} \left(\frac{10 \text{ cm}^{-3}}{n_H} \right)^{\frac{1}{2}} \left(\frac{0.01}{U} \right)^{\frac{1}{2}} \text{ kpc}, \quad (10)$$

where $\nu L_\nu(1500\text{\AA})$ is the monochromatic luminosity at 1500 Å, and we assume $n_e \approx n_H$ for an ionised gas. We estimate luminosities for each quasar using the g -band photometry from the Sloan Digital Sky Survey (SDSS). This provides a flux at rest wavelengths near 1500 Å, which we then extrapolate to 1500 Å using a power law with spectral index $\alpha_{OX} = -1.7$. We estimate the bolometric luminosity, L_{Bol} , for each quasar via integration of the SED, $\sim 6.76\nu L_\nu(1500\text{\AA})$ (Table 7). For Q0119–046, the derived density and $\log U \sim -1.9$ appropriate for the C II and Si II absorbing region yields a distance of $R \sim 5.7$ kpc (see Table 7). The errors listed for this distance derive from the uncertainty in U . For the other quasars, we combine the density upper limits with $\log U$ listed in Table 7 to derive conservatively small distance lower limits that range from $R \gtrsim 40$ to 330 kpc.

4.5 Gas Metallicity

We estimate metallicities only for component 2 in Q0119–046 where $N(\text{H I})$ is well measured. (The lower limits on $N(\text{H I})$ in the other quasars lead to large upper limits on

Table 7. Parameters of some absorbers. Columns show quasar name, bolometric luminosity in 10^{47} ergs s^{-1} , component, velocity shifts in km s^{-1} , column density ratio of C II* and C II, column density ratio of Si II* and Si II, electron density, ionisation parameter, total hydrogen column density, and radial distance in kpc.

QSO	L_{Bol} (10^{47} ergs s^{-1})	Component	v (km s^{-1})	$\frac{N(C\ II^*)}{N(C\ II)}$	$\frac{N(Si\ II^*)}{N(Si\ II)}$	$\log n_e$ (cm^{-3})	$\log U$	$\log N(H)$ (cm^{-2})	R (kpc)
Q0119–046	4.2	2	71 ± 202	1.9 ± 0.2	1.2 ± 0.3	3.4 ± 0.3	-1.9 ± 0.3 (Si II and Si III) 0.9 ± 0.3 (O VI and Ne VIII)	20.9 ± 0.4	$5.7^{+5.6}_{-2.8}$
Q0105+061	2.9	1	-2894 ± 507	< 0.2	< 0.5	< 0.7	-2.8 ± 0.3 (Si and C ions)	> 15.9	> 300
		2	-2858 ± 507	< 0.01	< 0.01	< 0.9	< -5 (Mg I) -3.0 ± 0.2 (Si and C ions) -1.8 ± 0.4 (C IV and N V)	> 15.9	> 300
		3	-2797 ± 507	< 0.05	< 0.1	< 1.9	< -5 (Mg I) -4.1 ± 0.2 (Si II and Si III)	> 14.5	> 331
		4	-2590 ± 507	< 0.3	< 0.6	< 0.9	-2.9 ± 0.2 (Si and C ions)	> 15.7	> 267
		5	-2544 ± 507	< 0.03	< 0.2	< 2.2	-2.6 ± 0.1 (Si ions)	> 16.6	> 41
		6	-2503 ± 507	< 0.01	< 0.03	< 1.4	-2.6 ± 0.3 (Si ions)	> 15.8	> 109
Q0334–204	3.4	1	-3035 ± 94	< 0.5	< 0.2	< 1.2	-2.2 ± 0.1 (Si and C ions) -1.2 ± 0.5 (C IV and O VI)	> 18.4	> 50
		2	-3006 ± 94	< 0.2	< 0.2	< 0.7	-2.3 ± 0.3 (Si and C ions) -1.3 ± 0.7 (C IV and O VI)	> 18.4	> 99
		3	-2991 ± 94	< 0.2	< 0.3	< 0.7	-2.6 ± 0.1 (Si and C ions) $-1.0^{+1.0}_{-0.6}$ (C IV and O VI)	> 18.0	> 140
Q2044–168	3.5	1	-2113 ± 102	< 0.5	—	< 1.2	-2.0 ± 0.2 (Si and C ions)	> 17.0	> 39
		2	-2042 ± 102	< 0.07	< 0.08	< 0.2	-2.4 ± 0.1 (Si and C ions) -1.8 ± 0.1 (C IV and N V)	> 16.8	> 198
		3	-1960 ± 102	< 0.2	—	< 0.7	-2.7 ± 0.2 (Si and C ions)	> 16.0	> 157
		4	-1929 ± 102	< 0.1	—	< 0.4	-2.5 ± 0.1 (Si and C ions) -1.8 ± 0.1 (C IV and N V)	> 16.6	> 176
		5	-1878 ± 102	< 0.3	—	< 0.9	-2.3 ± 0.1 (Si and C ions)	> 16.7	> 79

the metallicities, well above solar, that do not provide useful constraints.) The metallicity can be written generally as

$$\left[\frac{M}{H} \right] = \log \left(\frac{N(M_i)}{N(H\ I)} \right) + \log \left(\frac{f(H\ I)}{f(M_i)} \right) + \log \left(\frac{H}{M} \right)_{\odot}, \quad (11)$$

where $(H/M)_{\odot}$ is the solar abundance ratio of hydrogen to some metal M , $N(H\ I)$ and $f(H\ I)$ are the column density and ionisation fraction in $H\ I$, respectively, and $N(M_i)$ and $f(M_i)$ are the column density and ionisation fraction in some ion M_i of metal M .

To calculate $[Si/H]$ and $[C/H]$ for this absorber, we first use $\log U \approx -1.9$ obtained from the Si II and Si III region to determine the ionisation fractions $f(C\ II)$, $f(Si\ II)$, and $f(H\ I)$ from our calculation in Figure 9. Then the measured values of $N(Si\ II)$ and $N(C\ II)$ combined with $N(H\ I)$ indicate $[C/H] \approx -1.8 \pm 0.1$ and $[Si/H] \approx -2.4 \pm 0.2$. From Section 4.3, we know there is a range of ionization for this component. If assuming the high-ions O VI and Ne VIII have similar metallicity as the low-ions Si II and C II, then we use the $\log U \sim 0.9$ from the ratios O VI/Ne VIII, and the corresponding $f(H\ I) \sim -6.7$ and $f(O\ VI) \sim -1.4$ to predict $N(H\ I)$. The predicted $\log N(H\ I)$ is ~ 15.5 , which is much less than ~ 17.7 . This is the reason why we assume that the measured $H\ I$ column densities reside primarily with the lower metal ions (Section 4.3).

4.6 Spatial Structure and Cloud Survival

There is partial covering in roughly half of the components in Q0119–046. This implies that absorbers are not much larger (and probably smaller) than the projected area of the emission regions. The partial covering in C IV and Ly α appears to apply to the broad emission line region (BLR) because 1) these absorption lines sit on top of strong broad emission lines (Sargent, Boksenberg & Young 1982), 2) the covering fraction in C IV is only slightly less than Si IV, which does not sit on a strong emission line, and 3) the bottoms of the Ly α troughs are slanted in a way that is consistent with the peak of the broad Ly α emission line partially filling in the troughs. The BLR scaling relationship in (Bentz et al. 2013) indicate that the size of the broad emission region is ~ 1.0 pc, and therefore the absorbers have transverse size $\lesssim 1.0$ pc. We also find evidence for partial covering in O VI, Ne VIII and the higher Lyman lines. Since these features do not sit on strong emission lines, they must partially cover the much smaller continuum source. This requires the absorber sizes that are conservatively less than 0.01 pc (Netzer 1992; Hamann et al. 2011, Hamann et al., submitted).

These small cloud sizes in Q0119–046 are surprising given the derived radial distance of ~ 5.7 kpc, i.e., far for the quasar in the host galaxy. Such clouds are not expected

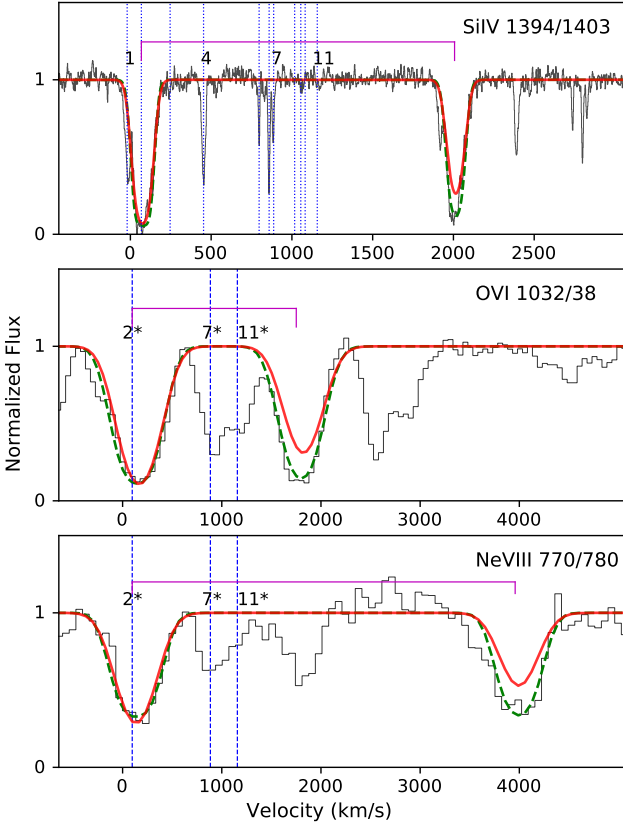


Figure 7. Observed spectra of Si IV $\lambda 1394$, 1403 (from Keck), O VI $\lambda 1032$, 1038 , and Ne VIII $\lambda 770$, 780 (from HST) of Q0119–046 (shown in black in each panel) are compared to predicted lines (component 2 or 2*) based on Si IV $\lambda 1394$, O VI $\lambda 1032$ and Ne VIII $\lambda 770$ assuming $C_0 = 1$ (red solid lines). The green dash lines in each panel show the final fitting results when $C_0 < 1$. The blue dash lines are components, and the brackets show the doublets. The velocities pertain to the short-wavelength lines in the doublets.

in a normal galactic interstellar medium, but they not unprecedented for distant AAL absorbing regions. For example, Hamann et al. (2001) found partial covering of the continuum source in an AAL absorber ~ 28 kpc from the central quasar. If the clouds are not confined by an external pressure, they will dissipate in roughly a sound crossing time (Hamann et al. 2001; Finn et al. 2014) given by

$$t_{sc} = \frac{l}{c_s}, \quad (12)$$

where c_s is the sound speed and l is the characteristic cloud size (Schaye 2001; Hamann et al. 2001; Finn et al. 2014). For a nominal temperature of 10^4 K and $l \lesssim 0.01$ pc or more conservatively $l \lesssim 1$ pc, the cloud survival times are $\lesssim 700$ yr or $\lesssim 70,000$ yr, respectively. The gas speeds in the various AAL systems in Q0119–046 are overall $\lesssim 1200$ km s $^{-1}$, which means that the cloud survival times are much shorter than any reasonable flow time we might assign to these absorbers. It therefore seems likely that the clouds were created in situ, at or near their observed location ~ 5.7 kpc from the quasar (see Section 5 for more discussion).

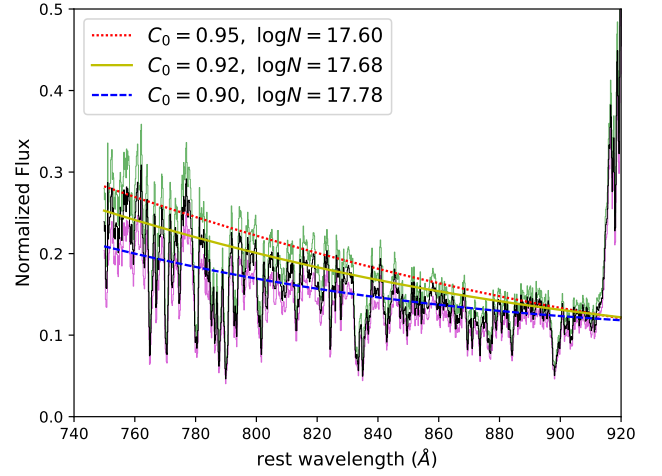


Figure 8. Observed spectrum normalized in three different ways using the continuum fits from Section 2.2.1 (Figure 1). Column densities values change with different covering fractions by fitting the Lyman limit. The green and mauve spectra are the upper and lower limits of the normalized spectra, respectively. And the black spectrum shows the best normalized spectrum. The dotted red and dashed dark blue lines are the upper and lower limits of fits considering uncertainties of normalization. The range of C_0 is 0.90 ($\log N = 17.78$) to 0.95 ($\log N = 17.60$). The best fit is $C_0 = 0.92$ and $\log N = 17.68$, shown as the solid yellow line.

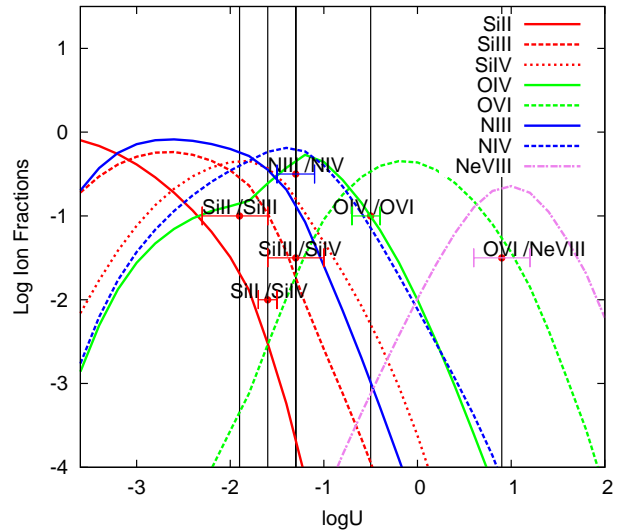


Figure 9. Theoretical ionisation fractions, $f(M_i)$, for selected stages of the elements Si, N, O and Ne plotted against different ionisation parameters $\log U$ for component 2 in Q0119–046. The black vertical lines with error bars are the best estimations of U for each ion pair.

5 DISCUSSION

The information derived in Sections 3 and 4 provides valuable constraints on the nature and origins of the AALs in our quasar sample. The results might have general relevance to high-redshift quasar environments, but it is important to

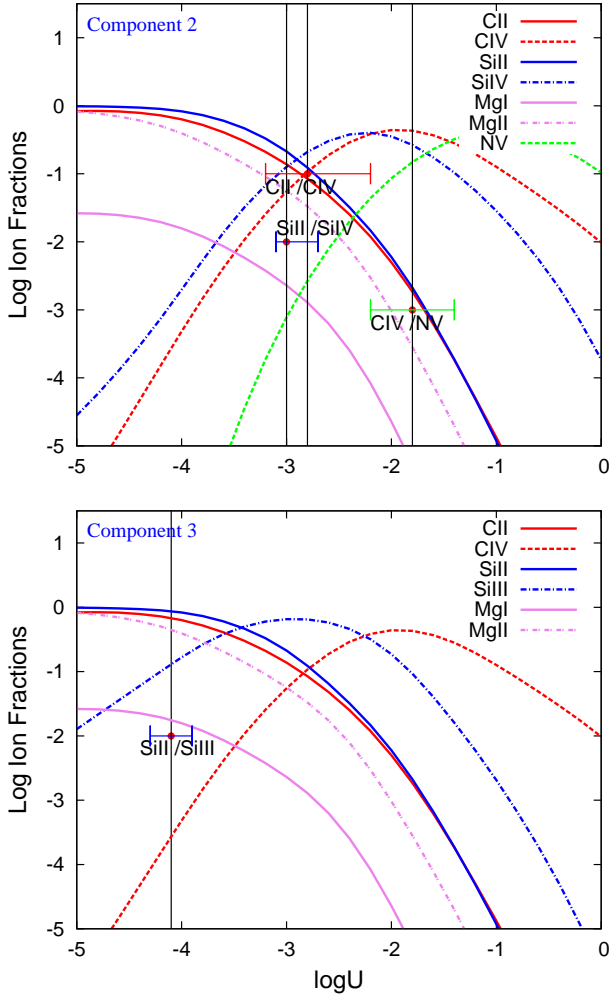


Figure 10. Theoretical ionisation fractions, $f(M_i)$, for selected stages of the elements Si, C, Mg and N plotted against different ionisation parameters $\log U$ for components 2 and 3 in Q0105+061. The black vertical lines with error bars are the best estimations of U for each ion pair.

keep in mind that the sample is biased. The quasars were selected to have rare low-ionisation lines (Si II and/or C II) useful for density and location constraints. More common types of AALs, with only higher-ionization lines, are not included in our sample. The full range of ions detected in our study, from Mg I, Mg II, Si II, C II, up to C IV, N V, and in some cases O VI and Ne VIII, often require a range of ionisation parameters in the AAL gas. If the diverse lines in each system form at roughly the same location, then the absorbing regions must span a range of densities. The most extreme case is component 2 in Q0119–046, where ions ranging from Si II to Ne VIII indicate a factor of ~ 630 range in densities (Section 4.3). This result is similar to several other quasars where measured Ne VIII AALs also indicate a range of ionisations and densities (Petitjean & Srianand 1999; Hamann, Netzer & Shields 2000; Hamann et al. 1995; Arav et al. 2013; Muzahid et al. 2013; Finn et al. 2014).

In our study, Q0119–046 has a unique dataset because we combine high-resolution spectra from Keck-HIRES with

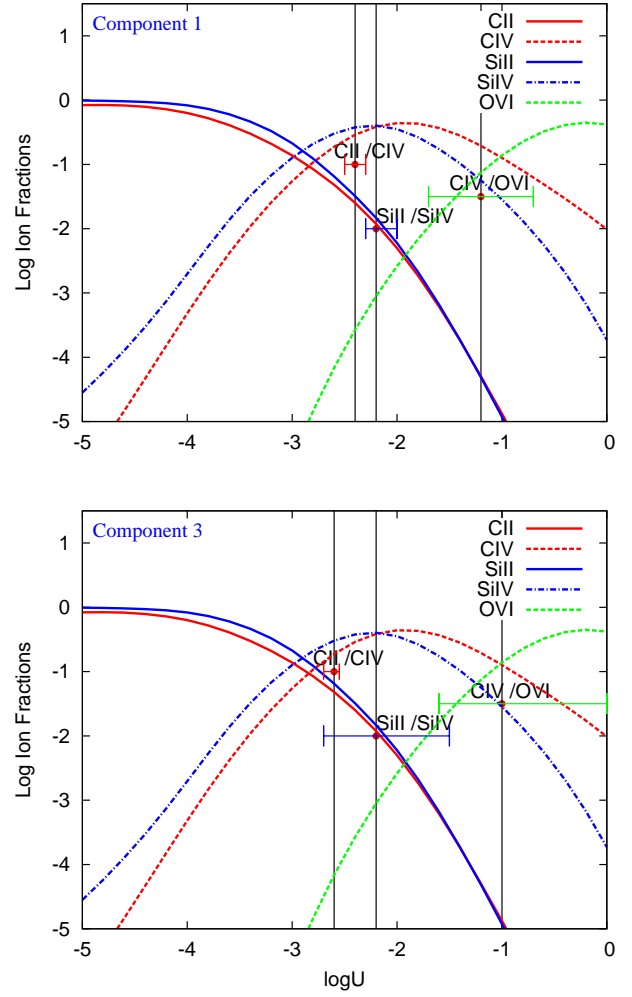


Figure 11. Theoretical ionisation fractions, $f(M_i)$, for selected stages of the elements Si, C and O plotted against different ionisation parameters $\log U$ for components 1 and 3 in Q0334–204. The black vertical lines with error bars are the best estimations of U for each ion pair.

spectra from HST-FOS that reach wavelengths down to ~ 750 Å in the quasar rest frame. These data provide the best measurements and different results than the other three AAL quasars in our sample. Thus we discuss Q0119–046 separately below.

5.1 Q0119–046

The AALs in Q0119–046 are clearly intrinsic to the quasar environment based on multiple components with partial covering of the background light source and high densities of $n_H \sim 2500 \text{ cm}^{-3}$ that lead to a derived distance of $R \sim 5.7$ kpc. These specific density and location results are similar to the absorbers studied by Dunn et al. (2010); Arav et al. (2013); Finn et al. (2014), which have $n_H \sim 1000$ to 6000 cm^{-3} and $R \sim 2$ to 6 kpc. The partial covering we find in Q0119–046 additionally implies that the absorber is composed of small clouds with characteristic sizes $\lesssim 1$ pc and possibly $\lesssim 0.01$ pc (if the partial covering applies to the continuum source,

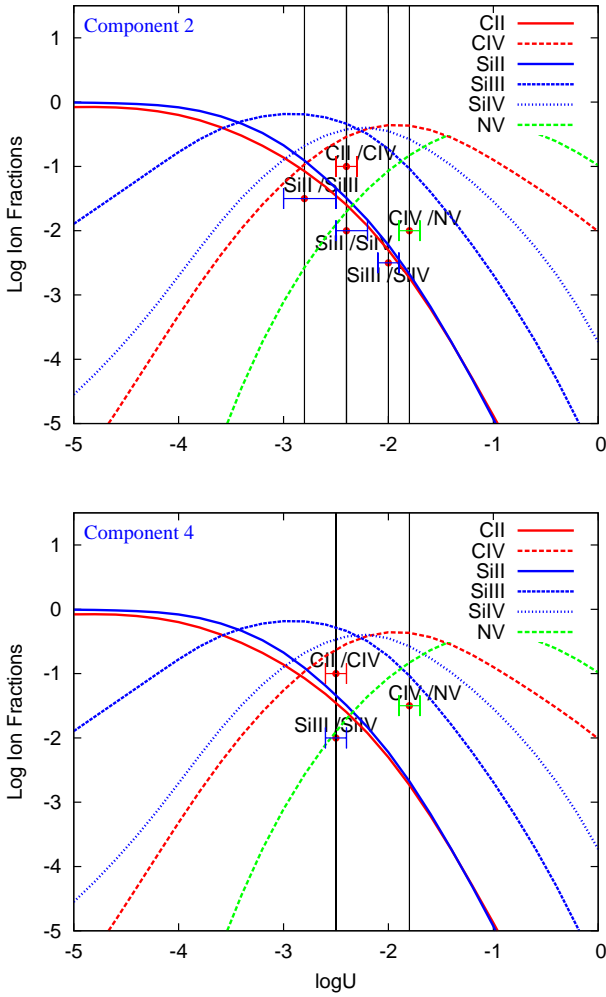


Figure 12. Theoretical ionisation fractions, $f(M_i)$, for selected stages of the elements Si, C and N plotted against different ionisation parameters $\log U$ for components 2 and 4 in Q2044-168. The black vertical lines with error bars are the best estimations of U for each ion pair.

Section 4.6). Our results overall are consistent with the previous study of Q0119-046 by Sargent, Boksenberg & Young (1982) that obtained only a lower limit on the density from C_{II}^*/C_{II} and an upper limit on the distance of <60 kpc. The AALs in Q0119-046 join a growing number of well-measured systems in other quasars where density indicators place the absorbers within the quasar environments but at large distances of a few to a few hundred kpc, and where partial covering of the quasar emission source can require small cloud sizes at these distances (see also Tripp, Lu & Savage 1996; Barlow & Sargent 1997; Srianand & Petitjean 2000; Hamann et al. 2001; Gabel, Arav & Kim 2006; Arav et al. 2008).

The radial distance $R \sim 5.7$ kpc of the absorber in Q0119-046 is an interesting location where a quasar-driven wind might be interacting with interstellar gas in the extended host galaxy. The derived metallicities in the range ~ 0.004 to $\sim 0.016 Z_{\odot}$ are substantially smaller than expected for an outflow originating in the galactic nuclear regions

near the quasar, where solar or higher metallicities should be present (Hamann & Ferland 1999; Arav et al. 2001; Hamann et al. 2002; Dietrich et al. 2003; Warner, Hamann & Dietrich 2004; Gabel et al. 2005; Nagao, Marconi & Maiolino 2006; Simon & Hamann 2010). If this AAL complex stems from a quasar-driven outflow, then the low metallicities might imply that the outflow gas is mixed with ambient interstellar gas in the galaxy. The multi-component nature of the AAL complex might identify interstellar clouds that have been shredded and dispersed by an unseen high-speed quasar-driven outflow, as described in some recent theoretical models (Hopkins & Elvis 2010; Faucher-Giguère & Kereš 2011; Faucher-Giguère, Quataert & Murray 2012). This interpretation is appealing because it provides a natural mechanism for creating small absorption-line clouds in situ, and thus avoiding the problem of their short survival times (see refs above, also Section 4.6).

However, another possibility is that the AAL absorbers in Q0119-046 represent infalling metal-poor gas from the intergalactic medium (IGM). The measured line velocities favor this infall interpretation. Components 1 and 2 have velocity shifts consistent with zero, while the other systems span a range of *positive* velocities from ~ 240 to ~ 1150 km s^{-1} (Table 2 and Section 2.1). In this infall scenario, small absorption-line clouds could be created in situ as condensations in larger reservoir of cold-mode accreting gas (Kereš et al. 2009; Fumagalli et al. 2011; Hafen et al. 2017). McCourt et al. (2016) describe theoretically that clouds of optically-thin, pressure-confined gas are inclined to fragment as they cool, reaching very small size scales of ~ 0.1 pc.

Accurate AAL velocity shifts are critical for this analysis. We adopt a redshift for Q0119-046 from Steidel & Sargent (1991) based on the Mg II broad emission line, with estimated measurement uncertainties of $\lesssim 100$ km s^{-1} (Section 2.1). Another possible source of uncertainty is the offset of the Mg II line from the true systemic rest frame of the quasar environment. Studies of large quasar samples indicate that the mean offset of the Mg II emission line relative to [O III] $\lambda 5007$ corresponds to a slight blueshift of ~ 100 km s^{-1} with 1σ scatter of ~ 270 km s^{-1} (Richards et al. 2002; Shen et al. 2007, 2016). If the [O III] line is a better redshift indicator, the probability for a random Mg II blueshifted matching our measured shift of ~ 1150 km s^{-1} is less than 0.005% ($\sim 4\sigma$). We conclude that at least some of the AAL components in Q0119-046 form in gas that is infalling toward the quasar.

Infalling gas (e.g., cold mode accretion) from the IGM is believed to be important during the early stages of galaxy formation to build mass, trigger star formation, and fuel the central black hole (Katz et al. 2003; Kereš et al. 2009, 2012). It is likely that infall and outflow occur together if cold-mode accretion is involved in triggering the starbursts and quasars that also drive feedback (Costa, Sijacki & Haehnelt 2014; Nelson et al. 2015; Suresh et al. 2015). Recent observations show that massive gas reservoirs are indeed present around high-redshift quasars, and that they are more extended and more massive around quasar hosts than similar inactive (non-quasar) galaxies (e.g., Prochaska, Lau & Hennawi 2014; Johnson, Chen & Mulchaey 2015; Martin et al. 2015, 2016; Borisova et al. 2016; Bouché et al. 2016; Ho et al. 2017). The nature of these gas reservoirs is poorly understood, but they are consistent with enhanced infall/cold-mode accretion from the IGM during an early active stage

of massive galaxy evolution when there is ongoing quasar activity. Quasar AALs can be valuable tracers of infall because they measure the gas speeds and physical conditions along radial lines of sight into galactic nuclei. The AALs in Q0119–046 might provide direct observational evidence for infall related to the assembly of a massive galaxy at redshift $z \sim 1.96$.

Compared to the work by [Sargent, Boksenberg & Young \(1982\)](#), we obtain more accurate results, especially $N(\text{H I})$ and $N(\text{H})$, based on the high-resolution Keck spectrum and more lines including the Lyman series and the Lyman limit from the HST spectrum. We estimate $n_{\text{H}} = 10^{3.4 \pm 0.3} \text{ cm}^{-3}$ via the strength ratio of $\text{Si II}^*/\text{Si II}$. While they constrained $n(\text{H}) > 100 \text{ cm}^{-3}$ based on the existence of excited state C II^* . The radial distance we obtain is ~ 5.7 kpc because of our accurate n_{H} estimates. While they estimated its radial distance to be less than 60 kpc by assuming $n_{\text{H}} > 100 \text{ cm}^{-3}$ and $N(\text{H}) = 10^{20} \text{ cm}^{-2}$. We find that $\sim 50\%$ of the absorbers show partial covering cases based on the lines C IV , Si IV , O VI , Ne VIII , Lyman series, and the Lyman limit. This requires absorber size scales less than 0.01 pc. While they did not find the partial covering cases. We find that the gas clouds are metal-poor and infalling at velocities from 0 to 1100 km s^{-1} by using the emission-line redshift obtained from Mg II . While they use the emission line C IV to obtain the systemic redshift, which leads to a smaller emission-line redshift than the real one, and thus they obtain a very large infalling speed of 2800 km s^{-1} for the absorber at $z_{\text{abs}} = 1.9644$. They guessed that the absorbers are analogous to the NGC 1275 high-velocity filaments ([Kent & Sargent 1979](#)). From our results, we conclude, because of these metal-poor, tiny (< 0.01 pc) absorbers and their short survival time (< 700 yr), they are created in situ, probably as condensations in cold-mode accreting gas or shredded IGM clouds that are dispersed by an unseen high-speed quasar-driven outflow. In addition, there seems to be no variation between the spectra of the two periods by visual comparisons, if the resolution difference is considered. The lack of variability is consistent with the absorber residing at kpc distances.

5.2 Q0105+061, Q0334–204, and Q2044–168

The AALs in the other three quasars in our sample, Q0105+061, Q0334–204, and Q2044–168, have velocity blueshifts consistent with outflows at speeds of -1900 to -3000 km s^{-1} . These systems do not exhibit partial covering of the background light source, and the upper limits we derive on their densities, $\lesssim 150$ to 15 cm^{-3} , place the absorbers at large distances from the quasars, namely, $\gtrsim 40$ to $\gtrsim 330$ kpc. Thus the relationship of the AAL systems to the quasars is not known. It is possible that they form in intervening gas that is not physically related to the quasars, such as galactic halos in the same galaxy cluster or group as the quasar host galaxies. However, previous statistical studies of large quasar samples indicate that ~ 80 percent of C IV AALs with rest equivalent width $\text{REW} \geq 0.3 \text{ \AA}$ at these velocity shifts form in quasar-driven outflows ([Misawa et al. 2007a](#); [Nestor, Hamann & Rodriguez Hidalgo 2008](#); [Wild et al. 2008](#); [Simon & Hamann 2010](#)).

If the AALs we measure do identify quasar outflows, then their speeds and minimum radial distances yield estimates of the minimum outflow masses and kinetic ener-

gies. We estimate the total masses assuming the absorbers are part of a spherical shell at distance R from the central quasar, namely

$$M = 4\pi\mu m_p Q R^2 N(\text{H}), \quad (13)$$

where Q is the global covering factor of the absorber as seen from the central quasar, m_p is the mass of a proton, and $\mu \sim 1.4$ is the mean molecular weight per proton in an ionized plasma with solar abundances ([Hamann 2000](#); [Hamann et al. 2001](#); [Dunn et al. 2010](#)). A rough estimate of Q is the incidence of associated absorbers generally in quasar spectra. Previous studies show that the incidence of AALs in radio-quiet quasars is around 20% ([Nestor, Hamann & Rodriguez Hidalgo 2008](#)). Therefore, we adopt $Q = 0.2$ to derive minimum total masses of $M \gtrsim (0.1 - 7.0) \times 10^7 M_{\odot}$ for the AAL absorbers in the three quasars. The corresponding minimum kinetic energies, given by $K = Mv^2/2$ are quite small, in the range $\sim (2.5 - 100) \times 10^{48} \text{ ergs s}^{-1}$. Dividing these energies by a characteristic flow time, $\Delta t \sim R/v$, yields kinetic energy rates, \dot{K} , that we compare to the bolometric luminosities (Section 4.4 and Table 7) to derive minimum ratios $\dot{K}/L_{\text{Bol}} \gtrsim 10^{-7}$ to 10^{-5} . The lower limits on these ratios are much too small to be important for feedback to the host galaxies, where $\dot{K}/L_{\text{Bol}} \gtrsim 0.05$ to 0.005 is believed to be required ([Scannapieco & Oh 2004](#); [Hopkins & Elvis 2010](#)). However, these estimates are based on conservative lower limits on $N(\text{H})$, which are 2 to 4 dex smaller than our reliable $N(\text{H})$ measurement for component 2 in Q0119–046.

We conclude that the AAL systems in these three quasars are likely to form in quasar-driven outflows, but their energies and potential for feedback to the host galaxies cannot be determined from existing data.

6 SUMMARY

We discuss rest-frame UV spectra of four redshift 2–3 quasars, Q0119–046, Q0105+061, Q0334–204, and Q2044–168, selected to have low-ionisation AALs in Si II and/or C II that are valuable to estimate electron densities and radial distances from the quasars. The data include high-resolution spectra obtained with Keck-HIRES or VLT-UVES that we combine, for Q0119–046 only, with an HST-FOS spectrum that reaches down to $\sim 750 \text{ \AA}$ in the quasar rest frame. Our analysis of Q0119–046 builds upon previous work on by [Sargent, Boksenberg & Young \(1982\)](#), but with higher-quality data and wavelength coverage that measures below the H I Lyman limit. The other three quasars were not previously studied. We fit every detected AAL to measure the gas kinematics, column densities, and line-of-sight covering fractions, and we estimate ionisations, total column densities, and radial distances using CLOUDY photoionisation models.

Our main results for Q0119–046 are the following:

1) The AALs in Q0119–046 identify a complex absorbing structure with at least 11 distinct velocity components. The velocity shifts of these components, ranging from ~ 0 to roughly $+1150 \text{ km s}^{-1}$ (relative to the Mg II emission line), are indicative of infall towards the quasar with estimated uncertainties of $\lesssim 200 \text{ km s}^{-1}$.

2) The electron density implied by the $\text{Si II}^*/\text{Si II}$ line

ratios in component 2, $n_e \sim 2500 \text{ cm}^{-3}$ (Section 4.1), indicates that this absorber resides at a distance ~ 5.7 kpc from the quasar (Section 4.4).

3) The wide range of ions detected in these AALs, from Si II up to Ne VIII, cannot be attributed to radiative shielding effects inside the absorber. It requires a range of densities from $\sim 2500 \text{ cm}^{-3}$ in the Si II region down to $\sim 4 \text{ cm}^{-3}$ in the Ne VIII gas *if* the lines all form at roughly the same radial distance (Sections 4.3 and 5.1).

4) The metallicities in AAL component 2 of Q0119–046 are in the range ~ 0.004 to ~ 0.016 times solar (Section 4.5).

5) Roughly half of the AAL components in Q0119–046 partially cover the background emission source (Section 4.6). This implies that the absorbers are composed of small clouds with characteristic sizes $\lesssim 1$ pc and possibly $\lesssim 0.01$ pc (based on O VI, Ne VIII and the higher Lyman lines that partially cover the quasar continuum source).

6) These tiny AAL clouds will have short survival times of $\lesssim 700$ yr or $\lesssim 70,000$ yr if they are not confined by an external pressure. At the derived distance of ~ 5.7 kpc, the cloud survival times are much less than a flow time, suggesting that the clouds are created in situ, at their observed location.

7) These results for Q0119–046 are consistent with models of galactic interstellar clouds being shredded and dispersed by a quasar-driven wind. However, the evidence for infall in the line shifts strongly favors an interpretation of this AAL complex as a series of condensations (spanning a factor of ~ 630 in density) embedded in a medium that is cold-mode accreting from the intergalactic medium (Section 5.1).

The other three quasars in our sample, Q0105+061, Q0334–204, Q2044–168, have AAL properties similar to each other but different from Q0119–046. Our main results for those quasars are the following:

1) Non-detections of the excited-state C II* and Si II* lines yield upper limits of electron densities from $n_e \lesssim 150$ to $\lesssim 15 \text{ cm}^{-3}$ and lower limits on the radial distances from $R \gtrsim 40$ to $\gtrsim 330$ kpc (Sections 4.1 and 4.4).

2) Most of the components in these AAL systems exhibit a range of ionizations, including the neutral Mg I $\lambda 2853$ line in Q0105+061. These ranges in ionization again require a range of densities within individual velocity components if the lines all form in roughly the same location (Section 4.3).

3) There is no evidence for partial covering in any of these AAL systems. Deep saturated lines in some of the components clearly indicate covering fractions of unity.

4) The AAL velocity shifts are indicative of outflows at speeds of ~ 1900 to $\sim 3000 \text{ km s}^{-1}$. Previous studies of large quasar samples indicate that ~ 80 percent of strong AALs in this velocity range do form in quasar outflows. These AALs might represent highly extended quasar-driven outflows, although the physical relationship of these particular AALs to the quasars cannot be determined (Section 5.2).

ACKNOWLEDGMENTS

We thank the anonymous referee for useful comments and suggestions. This work was supported by University of California, Riverside.

REFERENCES

- Anderson S. F., Weymann R. J., Foltz C. B., Chaffee, Jr. F. H., 1987, *AJ*, 94, 278
- Arav N., Borguet B., Chamberlain C., Edmonds D., Danforth C., 2013, *MNRAS*, 436, 3286
- Arav N. et al., 2001, *ApJ*, 561, 118
- Arav N., Kaastra J., Kriss G. A., Korista K. T., Gabel J., Proga D., 2005, *ApJ*, 620, 665
- Arav N., Korista K. T., de Kool M., 2002, *ApJ*, 566, 699
- Arav N., Moe M., Costantini E., Korista K. T., Benn C., Ellison S., 2008, *ApJ*, 681, 954
- Bahcall J. N., Wolf R. A., 1968, *ApJ*, 152, 701
- Barlow T. A., Hamann F., Sargent W. L. W., 1997, in *Astronomical Society of the Pacific Conference Series*, Vol. 128, *Mass Ejection from Active Galactic Nuclei*, Arav N., Shlosman I., Weymann R. J., eds., p. 13
- Barlow T. A., Sargent W. L. W., 1997, *AJ*, 113, 136
- Baskin A., Laor A., Stern J., 2014, *MNRAS*, 445, 3025
- Bentz M. C. et al., 2013, *ApJ*, 767, 149
- Borisova E., Lilly S. J., Cantalupo S., Prochaska J. X., Rakic O., Worseck G., 2016, *ApJ*, 830, 120
- Bouché N. et al., 2016, *ApJ*, 820, 121
- Chhetri R., Ekers R. D., Jones P. A., Ricci R., 2013, *MNRAS*, 434, 956
- Cicone C. et al., 2014, *A&A*, 562, A21
- Costa T., Sijacki D., Haehnelt M. G., 2014, *MNRAS*, 444, 2355
- de Kool M., Korista K. T., Arav N., 2002, *ApJ*, 580, 54
- Debuhr J., Quataert E., Ma C.-P., 2012, *MNRAS*, 420, 2221
- Di Matteo T., Springel V., Hernquist L., 2005, *Nature*, 433, 604
- Dietrich M., Hamann F., Shields J. C., Constantin A., Heidt J., Jäger K., Vestergaard M., Wagner S. J., 2003, *ApJ*, 589, 722
- D’Odorico V., Cristiani S., Romano D., Granato G. L., Danese L., 2004, *MNRAS*, 351, 976
- Dunn J. P. et al., 2010, *ApJ*, 709, 611
- Elvis M., 2006, *Memorie della Societa Astronomica Italiana*, 77, 573
- Faucher-Giguère C.-A., Kereš D., 2011, *MNRAS*, 412, L118
- Faucher-Giguère C.-A., Quataert E., Murray N., 2012, *MNRAS*, 420, 1347
- Ferland G. J. et al., 2013, *Rev. Mex. Astron. Astrofis.*, 49, 137
- Finn C. W. et al., 2014, *MNRAS*, 440, 3317
- Foltz C. B., Weymann R. J., Peterson B. M., Sun L., Malkan M. A., Chaffee, Jr. F. H., 1986, *ApJ*, 307, 504
- Fumagalli M., Prochaska J. X., Kasen D., Dekel A., Ceverino D., Primack J. R., 2011, *MNRAS*, 418, 1796
- Gabel J. R., Arav N., Kim T.-S., 2006, *ApJ*, 646, 742
- Gabel J. R. et al., 2005, *ApJ*, 631, 741
- Ganguly R., Eracleous M., Charlton J. C., Churchill C. W., 1999, *AJ*, 117, 2594
- Gaskell C. M., 1982, *ApJ*, 263, 79
- Hafen Z. et al., 2017, *MNRAS*, 469, 2292
- Hamann F., 1997, *ApJS*, 109, 279
- Hamann F., 2000, *Quasistellar Objects: Intrinsic AGN Absorption Lines*
- Hamann F., Barlow T., Cohen R. D., Junkkarinen V., Burbidge E. M., 1997a, in *Astronomical Society of the Pacific Conference Series*, Vol. 128, *Mass Ejection from Active Galactic Nuclei*, Arav N., Shlosman I., Weymann R. J., eds., pp. 19–+
- Hamann F., Barlow T. A., Beaver E. A., Burbidge E. M., Cohen R. D., Junkkarinen V., Lyons R., 1995, *ApJ*, 443, 606
- Hamann F., Barlow T. A., Junkkarinen V., 1997, *ApJ*, 478, 87
- Hamann F., Barlow T. A., Junkkarinen V., Burbidge E. M., 1997b, *ApJ*, 478, 80
- Hamann F., Chartas G., McGraw S., Rodriguez Hidalgo P., Shields J., Capellupo D., Charlton J., Eracleous M., 2013, *MNRAS*, 435, 133
- Hamann F., Ferland G., 1999, *ARA&A*, 37, 487

- Hamann F., Kanekar N., Prochaska J. X., Murphy M. T., Ellison S., Malec A. L., Milutinovic N., Ubachs W., 2011, *MNRAS*, 410, 1957
- Hamann F., Korista K. T., Ferland G. J., Warner C., Baldwin J., 2002, *ApJ*, 564, 592
- Hamann F., Sabra B., 2004, in *Astronomical Society of the Pacific Conference Series*, Vol. 311, *AGN Physics with the Sloan Digital Sky Survey*, Richards G. T., Hall P. B., eds., pp. 203–+
- Hamann F. W., Barlow T. A., Chaffee F. C., Foltz C. B., Weymann R. J., 2001, *ApJ*, 550, 142
- Hamann F. W., Netzer H., Shields J. C., 2000, *ApJ*, 536, 101
- Ho S. H., Martin C. L., Kacprzak G. G., Churchill C. W., 2017, *ApJ*, 835, 267
- Hopkins P. F., Elvis M., 2010, *MNRAS*, 401, 7
- Hopkins P. F., Hernquist L., Cox T. J., Kereš D., 2008, *ApJS*, 175, 356
- Hopkins P. F., Richards G. T., Hernquist L., 2007, *ApJ*, 654, 731
- Hopkins P. F., Torrey P., Faucher-Giguère C.-A., Quataert E., Murray N., 2016, *MNRAS*, 458, 816
- Johnson S. D., Chen H.-W., Mulchaey J. S., 2015, *MNRAS*, 452, 2553
- Katz N., Kereš D., Dave R., Weinberg D. H., 2003, in *Astrophysics and Space Science Library*, Vol. 281, *The IGM/Galaxy Connection. The Distribution of Baryons at z=0*, Rosenberg J. L., Putman M. E., eds., p. 185
- Kauffmann G., Haehnelt M., 2000, *MNRAS*, 311, 576
- Kent S. M., Sargent W. L. W., 1979, *ApJ*, 230, 667
- Kereš D., Katz N., Fardal M., Davé R., Weinberg D. H., 2009, *MNRAS*, 395, 160
- Kereš D., Vogelsberger M., Sijacki D., Springel V., Hernquist L., 2012, *MNRAS*, 425, 2027
- King A., 2003, *ApJ*, 596, L27
- Leighly K. M., Dietrich M., Barber S., 2011, *ApJ*, 728, 94
- Martin D. C., Matuszewski M., Morrissey P., Neill J. D., Moore A., Cantalupo S., Prochaska J. X., Chang D., 2015, *Nature*, 524, 192
- Martin D. C., Matuszewski M., Morrissey P., Neill J. D., Moore A., Steidel C. C., Trainor R., 2016, *ApJ*, 824, L5
- McCourt M., Oh S. P., O’Leary R. M., Madigan A.-M., 2016, *ArXiv e-prints*
- Misawa T., Charlton J. C., Eracleous M., Ganguly R., Tytler D., Kirkman D., Suzuki N., Lubin D., 2007a, *ApJS*, 171, 1
- Misawa T., Eracleous M., Charlton J. C., Kashikawa N., 2007b, *ApJ*, 660, 152
- Morris S. L., Weymann R. J., Foltz C. B., Turnshek D. A., Shectman S., Price C., Boroson T. A., 1986, *ApJ*, 310, 40
- Murphy T. et al., 2010, *MNRAS*, 402, 2403
- Muzahid S., Srianand R., Arav N., Savage B. D., Narayanan A., 2013, *MNRAS*, 431, 2885
- Nagao T., Marconi A., Maiolino R., 2006, *A&A*, 447, 157
- Narayanan D., Hamann F., Barlow T., Burbidge E. M., Cohen R. D., Junkkarinen V., Lyons R., 2004, *ApJ*, 601, 715
- Nelson D., Genel S., Vogelsberger M., Springel V., Sijacki D., Torrey P., Hernquist L., 2015, *MNRAS*, 448, 59
- Nestor D., Hamann F., Rodriguez Hidalgo P., 2008, *MNRAS*, 386, 2055
- Netzer H., 1992, in *American Institute of Physics Conference Series*, Vol. 254, *American Institute of Physics Conference Series*, Holt S. S., Neff S. G., Urry C. M., eds., pp. 146–154
- Osterbrock D. E., 1989, *Astrophysics of gaseous nebulae and active galactic nuclei*
- Ostriker J. P., Choi E., Ciotti L., Novak G. S., Proga D., 2010, *ApJ*, 722, 642
- Perrotta S. et al., 2016, *MNRAS*, 462, 3285
- Petitjean P., Srianand R., 1999, *A&A*, 345, 73
- Prochaska J. X., Lau M. W., Hennawi J. F., 2014, *ApJ*, 796, 140
- Rauch M., 1998, *ARA&A*, 36, 267
- Reeves J. N., Turner M. J. L., 2000, *MNRAS*, 316, 234
- Richards G. T. et al., 2006, *ApJS*, 166, 470
- Richards G. T., Vanden Berk D. E., Reichard T. A., Hall P. B., Schneider D. P., SubbaRao M., Thakar A. R., York D. G., 2002, *AJ*, 124, 1
- Robson E. I., Gear W. K., Smith M. G., Ade P. A. R., Nolt I. G., 1985, *MNRAS*, 213, 355
- Rupke D. S. N., Gültekin K., Veilleux S., 2017, *ApJ*, 850, 40
- Rupke D. S. N., Veilleux S., 2013, *ApJ*, 768, 75
- Sanders D. B., Soifer B. T., Elias J. H., Madore B. F., Matthews K., Neugebauer G., Scoville N. Z., 1988, *ApJ*, 325, 74
- Sargent W. L. W., Boksenberg A., Young P., 1982, *ApJ*, 252, 54
- Scannapieco E., Oh S. P., 2004, *ApJ*, 608, 62
- Schaye J., 2001, *ApJ*, 559, 507
- Schaye J., Carswell R. F., Kim T.-S., 2007, *MNRAS*, 379, 1169
- Schneider D. P. et al., 1993, *ApJS*, 87, 45
- Shen Y. et al., 2016, *ApJ*, 831, 7
- Shen Y. et al., 2007, *AJ*, 133, 2222
- Shull J. M., Stevans M., Danforth C. W., 2012, *ApJ*, 752, 162
- Silk J., Rees M. J., 1998, *A&A*, 331, L1
- Simon L., 2011, *High Redshift Quasar Abundances and Environments: Connecting Black Hole and Host Galaxy Evolution*. University of Florida
- Simon L. E., Hamann F., 2010, *MNRAS*, 407, 1826
- Simon L. E., Hamann F., Pettini M., 2012, in *Astronomical Society of the Pacific Conference Series*, Vol. 460, *AGN Winds in Charleston*, Chartas G., Hamann F., Leighly K. M., eds., p. 52
- Sramek R. A., Weedman D. W., 1980, *ApJ*, 238, 435
- Srianand R., Petitjean P., 2000, *A&A*, 357, 414
- Steidel C. C., Sargent W. L. W., 1991, *ApJ*, 382, 433
- Suresh J., Bird S., Vogelsberger M., Genel S., Torrey P., Sijacki D., Springel V., Hernquist L., 2015, *MNRAS*, 448, 895
- Tayal S. S., 2008a, *ApJS*, 179, 534
- Tayal S. S., 2008b, *VizieR Online Data Catalog*, 348
- Tripp T. M., Lu L., Savage B. D., 1996, *ApJS*, 102, 239
- Tytler D., Fan X.-M., 1992, *ApJS*, 79, 1
- Tytler D., O’Meara J. M., Suzuki N., Kirkman D., Lubin D., Orin A., 2004, *AJ*, 128, 1058
- Ulrich M.-H., 1989, *A&A*, 220, 71
- Veilleux S. et al., 2009, *ApJ*, 701, 587
- Wang H., Wang T., Zhou H., Liu B., Wang J., Yuan W., Dong X., 2011, *ApJ*, 738, 85
- Warner C., Hamann F., Dietrich M., 2004, *ApJ*, 608, 136
- Weymann R. J., Morris S. L., Foltz C. B., Hewett P. C., 1991, *ApJ*, 373, 23
- Weymann R. J., Williams R. E., Peterson B. M., Turnshek D. A., 1979, *ApJ*, 234, 33
- Wild V. et al., 2008, *MNRAS*, 388, 227
- Wise J. H., Eracleous M., Charlton J. C., Ganguly R., 2004, *ApJ*, 613, 129